




上节课回顾

4.3 中尺度对流系统的前沿进展： 观测

A satellite image of Earth from space, showing a large-scale atmospheric circulation system over the ocean. The system is characterized by a central core of dense, dark clouds, surrounded by a spiral of lighter, wispy clouds. The ocean surface is visible in shades of blue, and the Earth's horizon is visible at the top of the frame.

The formation, character and changing nature of mesoscale convective systems

Russ S. Schumacher   and Kristen L. Rasmussen

Abstract | Mesoscale convective systems (MCSs) describe organized groupings of thunderstorms in the tropics and mid-latitudes that span thousands of square kilometres. While recognized for over a century, the advent of satellite and radar observations, as well as atmospheric-model simulations, has brought about their increased understanding. In this Review, we synthesize current knowledge on MCS formation, climatological characteristics, hazardous weather, predictive capacity and projected changes with anthropogenic warming. Driven by typical deep moist convective processes (moisture, lift and instability) and vertical wind shear, MCS formation occurs preferentially in locations where these ingredients are present and can be maintained by large-scale ascent and the cold pools that they produce. MCSs also generate hazardous weather, including extreme rainfall, flooding, derechos and, sometimes, tornadoes and hail, all of which have substantial economic and societal impacts. Given that MCSs also produce a large fraction of warm-season rainfall, there is critical need for both short-term forecasts and long-term projections, presently challenged by inadequate model resolution. Yet, with continually improving modelling capabilities, as well as greater theoretical basis, it is suggested that MCSs might increase in frequency and intensity under a warming climate. Further modelling progress, in turn, offers improved understanding of MCS characteristics, from their life cycle through to impacts.

上节课回顾

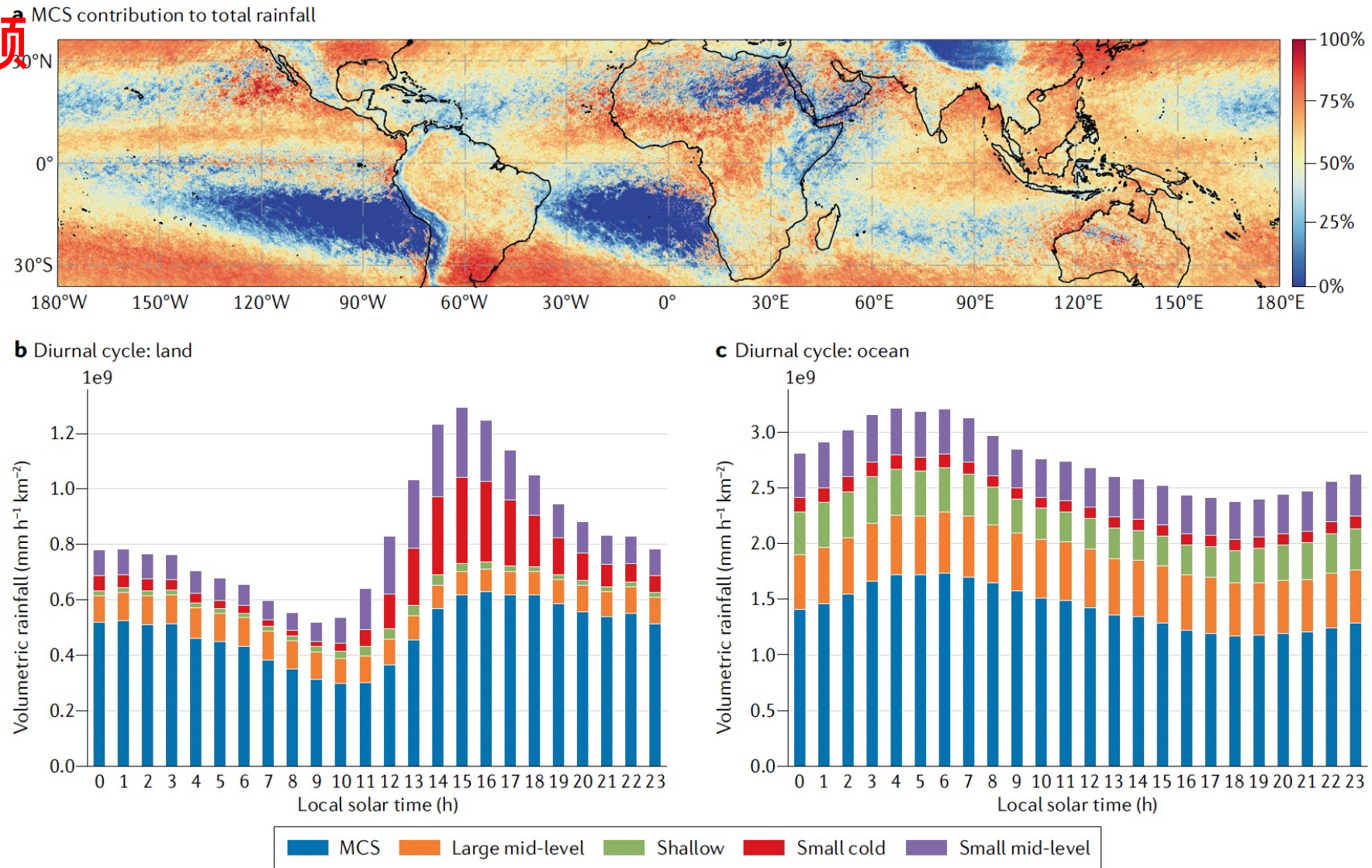


Fig. 2 | **The contribution of MCSs to global rainfall.** Fraction of annual rainfall produced by mesoscale convective systems (MCSs) based on observations from the Tropical Rainfall Measuring Mission (TRMM) satellite between December 1997 and September 2014 (panel a). Diurnal cycle of TRMM volumetric rainfall over the land (panel b) and ocean (panel c) between 36°N/S. In many parts of the global tropics, subtropics and mid-latitudes, MCSs produce a large fraction of the annual precipitation. MCSs over land have a strong diurnal cycle, with rain maximized in the afternoon and evening, and minimized in the morning; MCSs over ocean have a less pronounced diurnal cycle. Panel a adapted with permission from REF.⁶, © American Meteorological Society. Panels b and c adapted with permission from REF.⁵⁰, © American Meteorological Society.

JGR Atmospheres



RESEARCH ARTICLE

10.1029/2020JD034202

Key Points:

- Develop an algorithm to track mesoscale convective systems globally using satellite infrared brightness temperature and precipitation data
- Satellite-based tracking reproduces mesoscale convective system statistics derived from tracking using ground-based radar network data

A Global High-Resolution Mesoscale Convective System Database Using Satellite-Derived Cloud Tops, Surface Precipitation, and Tracking

Zhe Feng¹ , L. Ruby Leung¹ , Nana Liu¹ , Jingyu Wang¹ , Robert A. Houze Jr², Jianfeng Li¹ , Joseph C. Hardin¹ , Dandan Chen³, and Jianping Guo³ 

¹Division of Atmospheric Sciences and Global Change, Pacific Northwest National Laboratory, Richland, WA, USA, ²Department of Atmospheric Sciences, University of Washington, Seattle, WA, USA, ³State Key Laboratory of Severe Weather, Chinese Academy of Meteorological Sciences, Beijing, China

上节课回顾

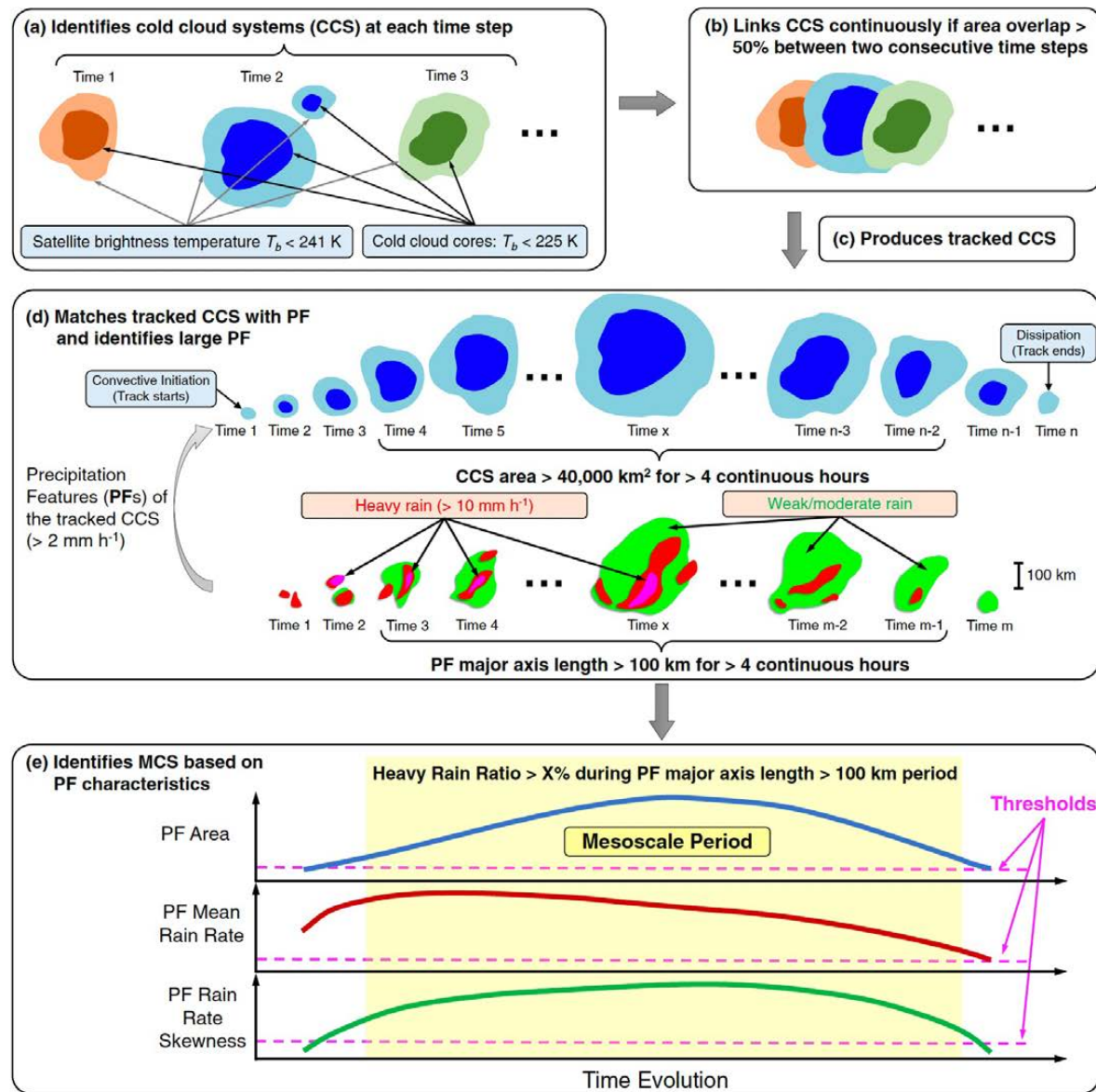


Figure 1. Schematic flowchart of MCS identification using collocated satellite infrared brightness temperature (T_b) and precipitation observations in this study. (a) Identification of cold cloud system (CCS) based on T_b signatures, (b) tracking of CCS between two consecutive times, (c) linking all consecutive times to produce tracks, (d) matches tracked CCS with associated precipitation feature (PF), and (e) identification of MCS based on PF characteristics. The yellow shading in (e) denotes the mesoscale period as defined by CCS $> 40,000$ km², with a PF major axis length larger than 100 km for longer than four continuous hours. During this period, the PF area, mean rain rate, and rain rate skewness must exceed the thresholds denoted by the magenta dash lines, and the heavy rain volume ratio during this period must be larger than X% (a function of lifetime, see Figure 3) to qualify as an MCS. See text for more details. MCS, Mesoscale convective system.

Geophysical Research Letters®



RESEARCH LETTER

10.1029/2023GL103595

Key Points:

- Mesoscale convective systems (MCSs) have become more frequent and intense in the East Asian rainband over the past two decades
- The significant increase of MCS precipitation accounted for three quarters of the total rainfall increase during 2000–2021
- The increase of atmospheric total column water vapor, mainly driven by anthropogenic forcing, leads to more favorable environments for MCSs

Intensification of Mesoscale Convective Systems in the East Asian Rainband Over the Past Two Decades

Puxi Li¹ , **Fengfei Song^{2,3}** , **Haoming Chen¹**, **Jian Li¹** , **Andreas F. Prein⁴** , **Wenxia Zhang⁵** , **Tianjun Zhou⁵**, **Moran Zhuang^{6,7}**, **Kalli Furtado⁸** , **Mark Muetzelfeldt⁹**, **Reinhard Schiemann⁹** , and **Chao Li¹⁰**

¹State Key Laboratory of Severe Weather, Chinese Academy of Meteorological Sciences, China Meteorological Administration, Beijing, China, ²Frontier Science Center for Deep Ocean Multispheres and Earth System and Physical Oceanography Laboratory, Ocean University of China, Qingdao, China, ³Laoshan Laboratory, Qingdao, China, ⁴National Center for Atmospheric Research, Boulder, CO, USA, ⁵LASG, Institute of Atmospheric Physics, Chinese Academy of Sciences, Beijing, China, ⁶CMA Earth System Modeling and Prediction Centre, China Meteorological Administration, Beijing, China, ⁷Key Laboratory of Earth System Modeling and Prediction, China Meteorological Administration, Beijing, China, ⁸Met Office, Exeter, UK, ⁹National Centre for Atmospheric Science, Department of Meteorology, University of Reading, Reading, UK, ¹⁰Max Planck Institute for Meteorology, Hamburg, Germany

上节课回顾

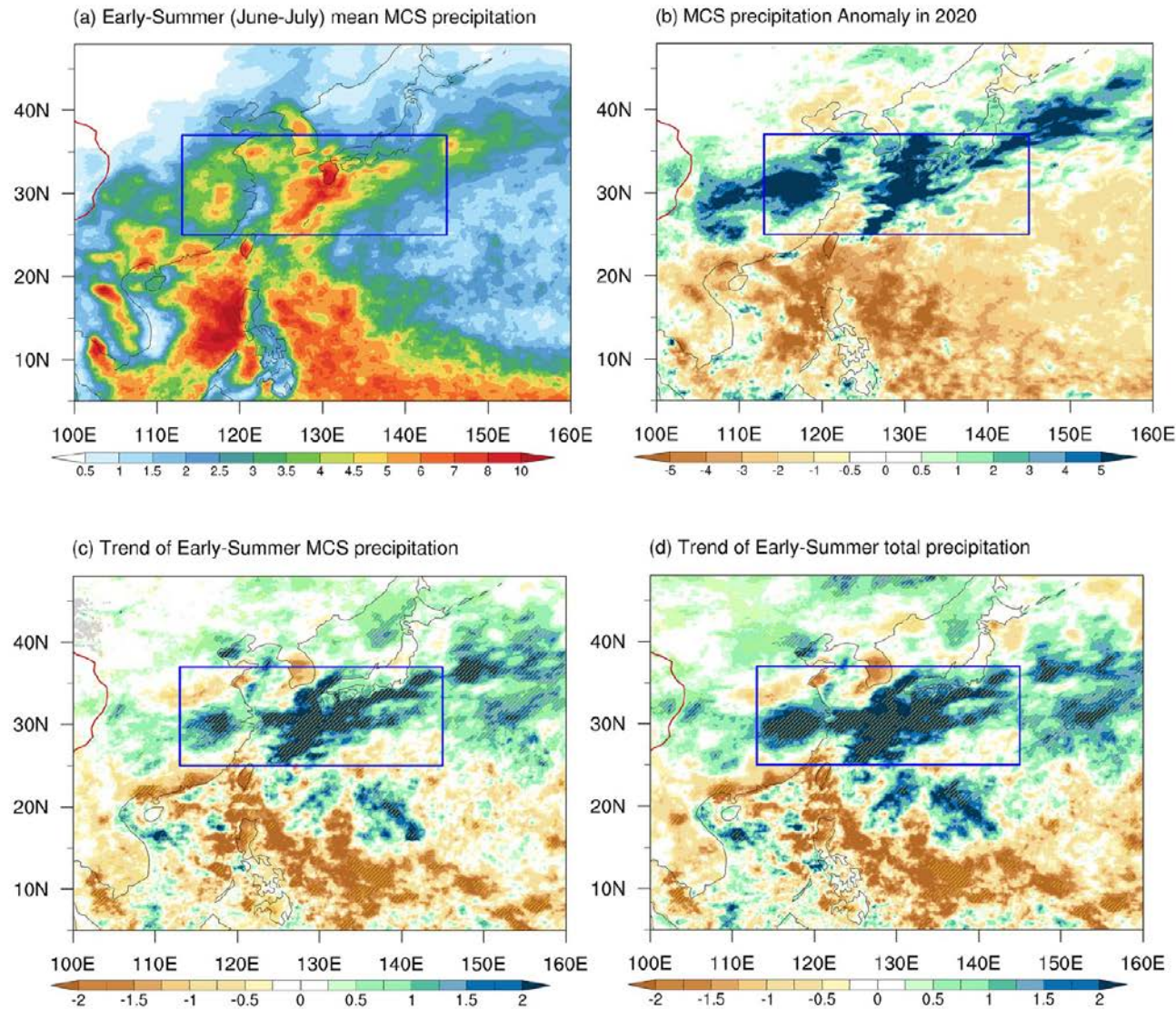


Figure 1. Mesoscale convective systems (MCSs) contributed the majority of the increasing trend of total precipitation in early summer over East Asia during the past two decades (from 2000 to 2021). (a) Early-summer MCS precipitation climatology (unit: mm day⁻¹). (b) Early-summer MCS precipitation anomalies in 2020 (unit: mm day⁻¹). (c) The MCS precipitation trend during the past two decades (unit: mm day⁻¹ decade⁻¹). (d) The same as (c), but for the total precipitation trend. Grid points with a statistical significance exceeding the 95% confidence level (with a two-tailed Student's *t*-test) are marked by yellow diagonal lines. The red contour indicates the Tibetan Plateau (the topography exceeds 2,700 m). The blue boxes indicate the target domain (the East Asian rainband), where the statistical analyses have been performed.

上节课回顾

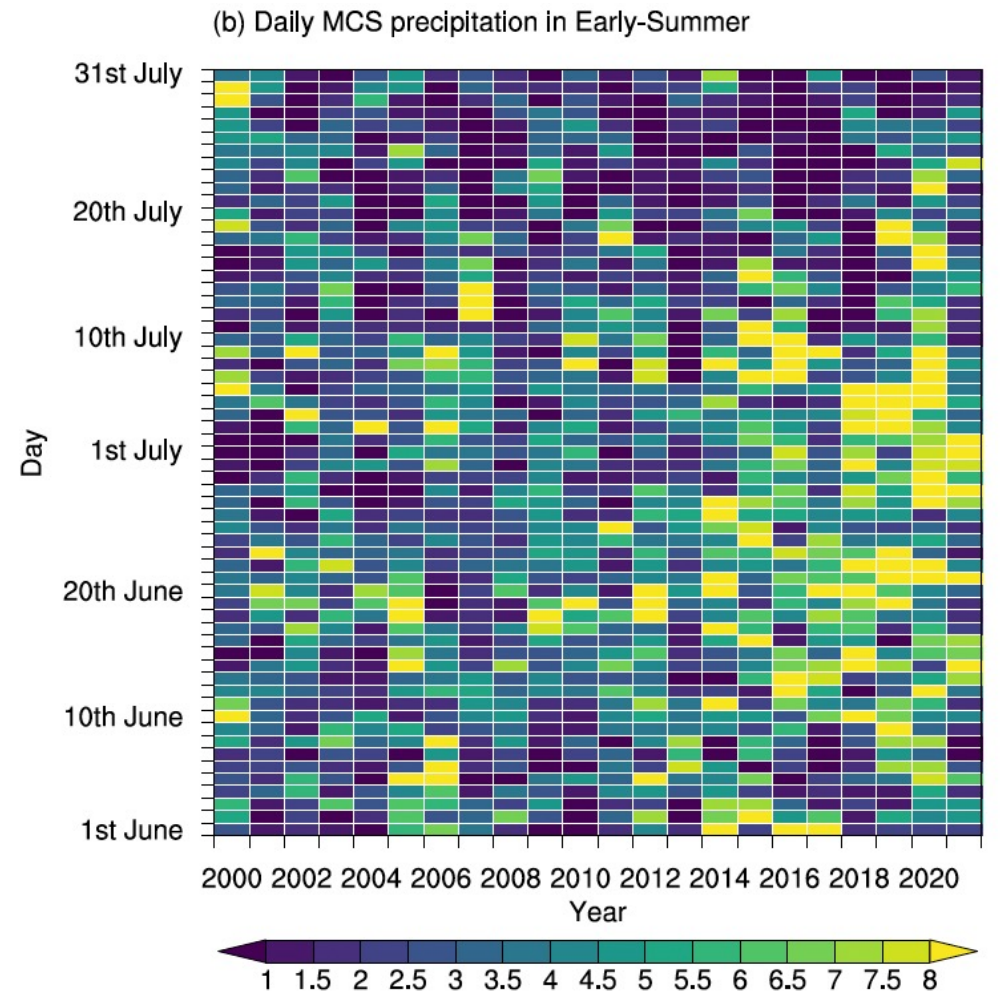
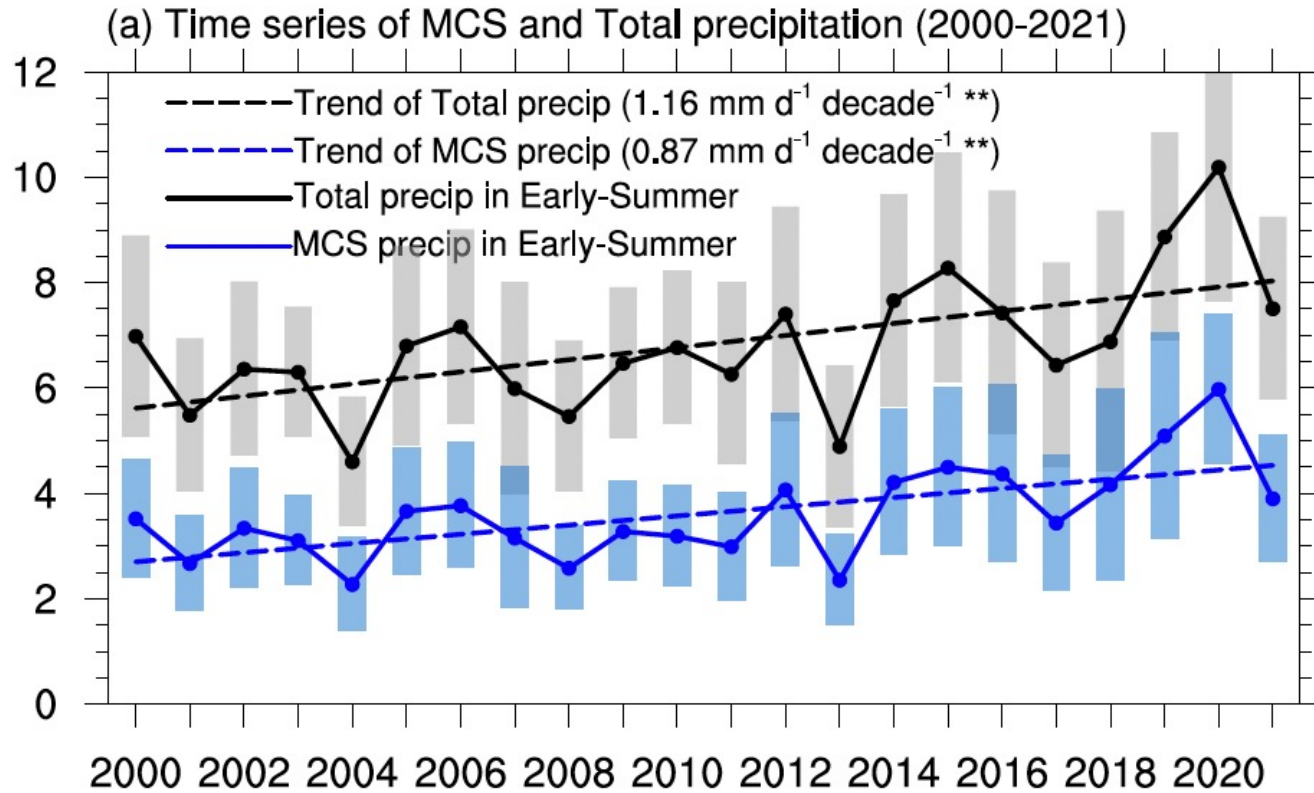


Figure 2. Time series and linear trends of MCS and total precipitation, and daily mean MCS precipitation within each early-summer season over the East Asian rainband. (a) Time series of early-summer MCS (blue) and total (black) precipitation (unit: mm day^{-1}), and linear trends of MCS (blue dashed line) and total precipitation (black dashed line; both statistically significant at 99% with two-tailed Student's t -tests) of early summer (unit: $\text{mm day}^{-1} \text{ decade}^{-1}$). Here the gray/blue shadings represent the ± 0.5 standard deviations of the daily total/MCS precipitation in each early-summer. (b) Daily mean MCS precipitation (unit: mm day^{-1}) within each early-summer season during the past two decades (2000–2021).

上节课回顾

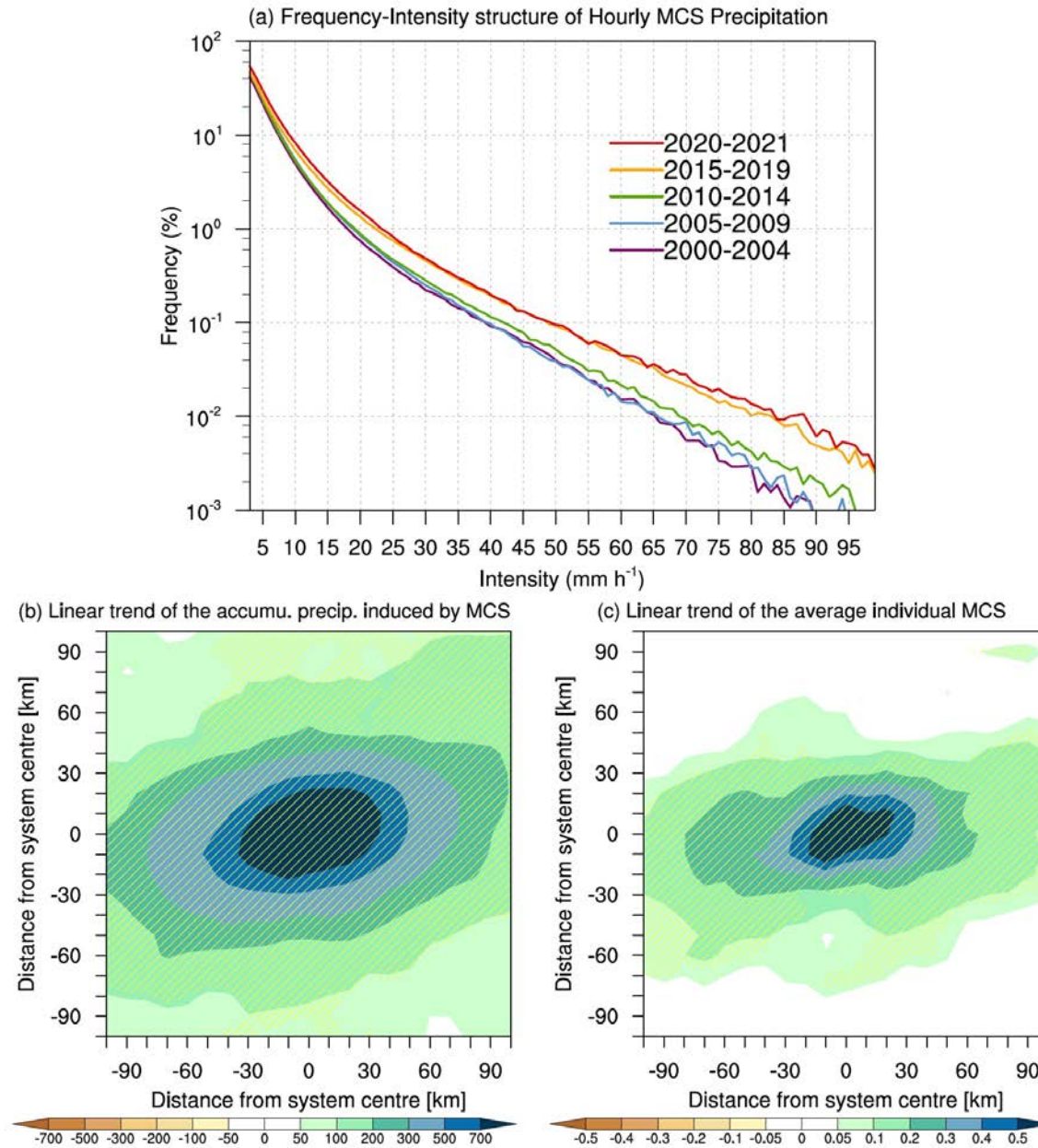

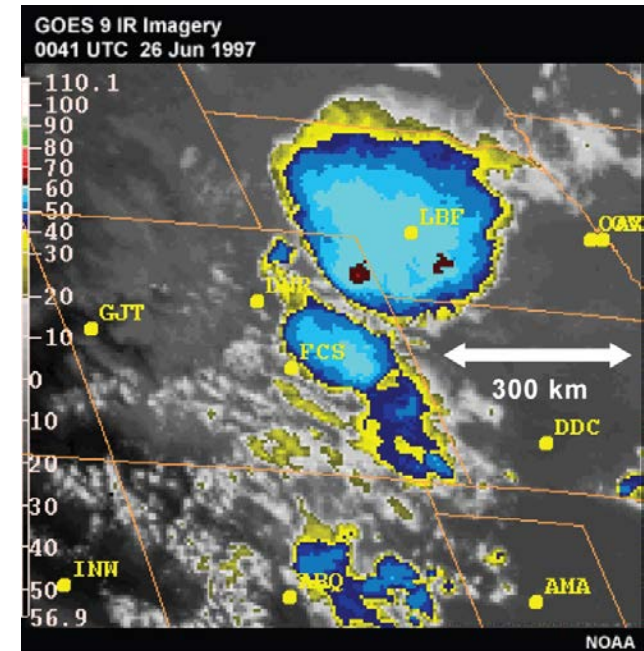
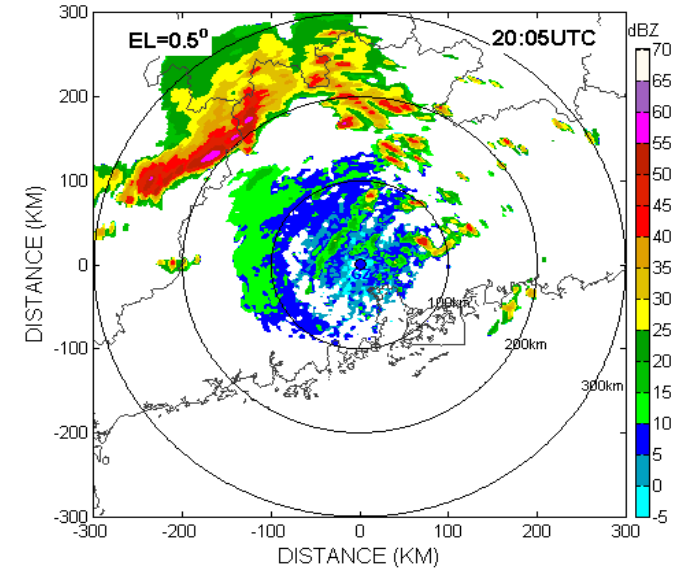
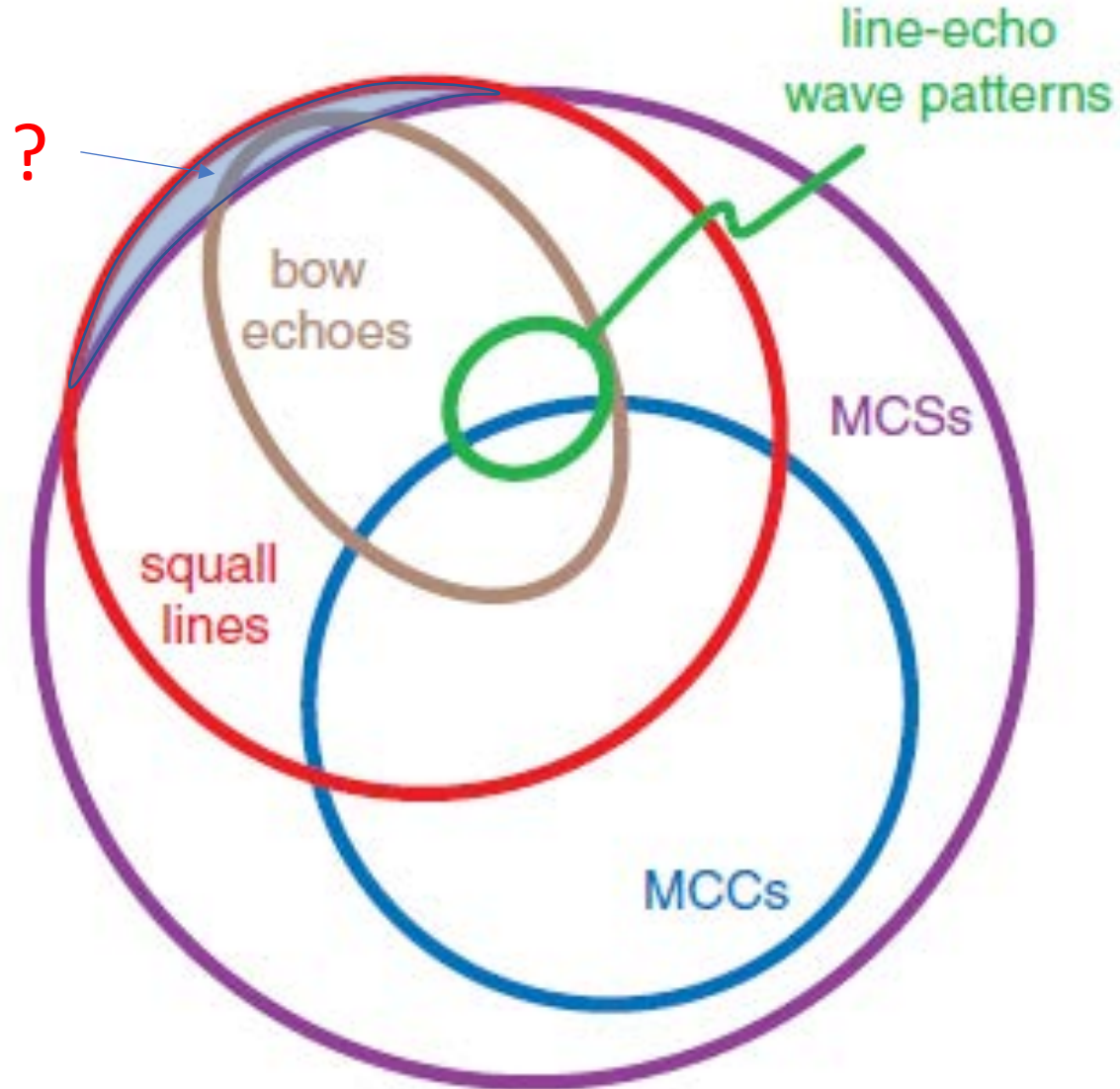


Figure 3. Probability density function of MCS hourly precipitation, and linear trends of the accumulated amount and the composited precipitation averages according to the location of the MCS precipitation center. (a) Frequency-Intensity structure of MCS hourly precipitation over the East Asian rainband. Linear trends of the (b) composited accumulated rainfall amount (unit: mm decade⁻¹) produced by all MCS and (c) hourly precipitation averages of each individual MCS (unit: mm h⁻¹ decade⁻¹) in each early-summer season from 2000 to 2021. Grid points with a statistical significance exceeding the 95% confidence level are marked by yellow diagonal lines, with two-tailed Student's *t*-tests.

A satellite view of Earth from space, showing a large, well-defined cyclone system over the ocean. The cyclone has a distinct eye and spiral cloud bands. The surrounding ocean is a deep blue, and the atmosphere is visible as a thin blue layer. The text is overlaid in the center of the image.

4.4 中尺度对流系统的前沿进展： 理论与模拟

Relationships among Sub-classifications of MCSs



胞线的流场

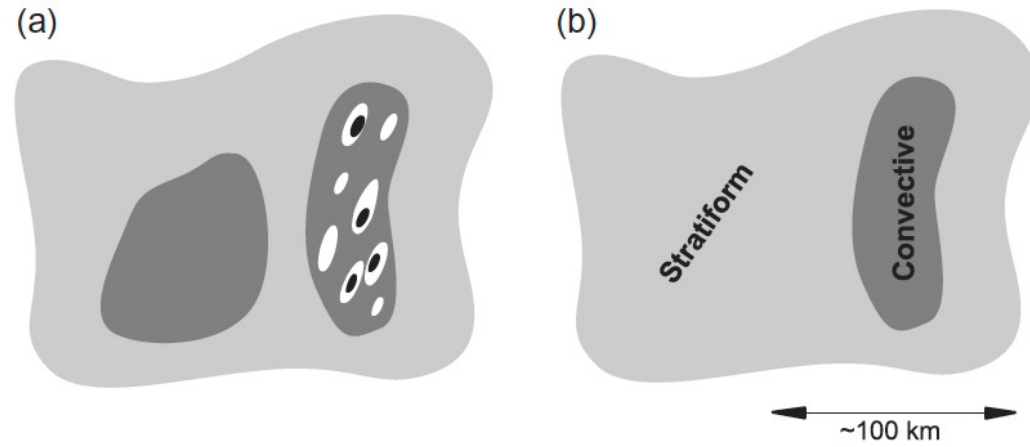


FIGURE 9.4 (a) Idealization of a horizontal map of radar reflectivity in an MCS. (b) Reflectivity divided into convective and stratiform regions. From Houze (1997). Republished with permission of the American Meteorological Society.

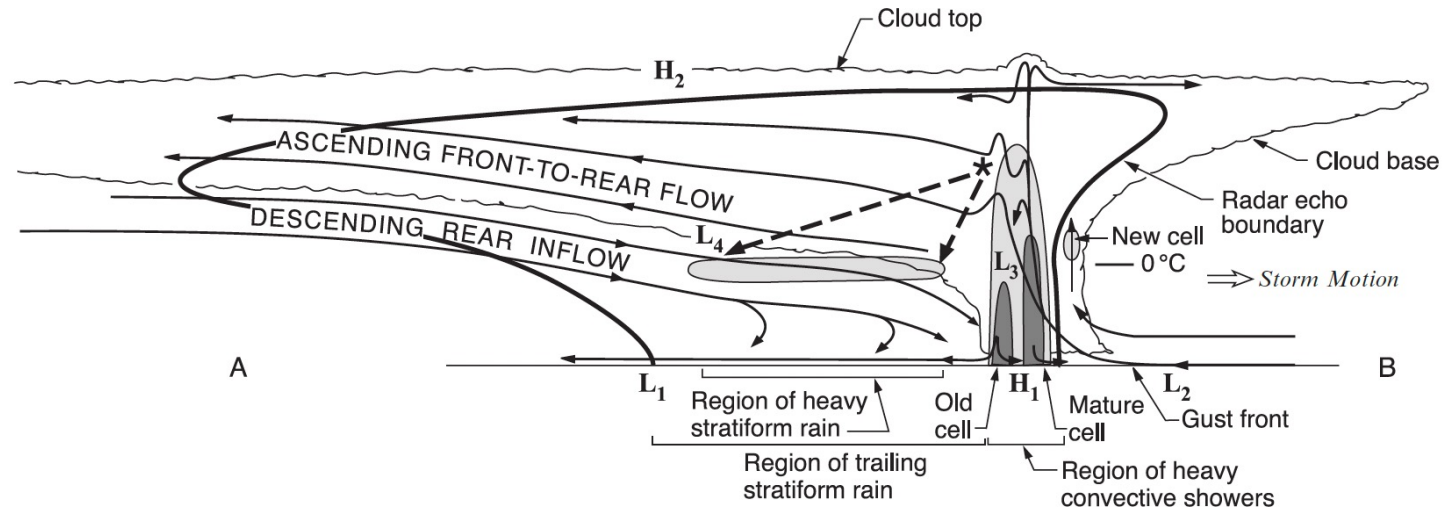


FIGURE 9.15 Conceptual model of the kinematic, microphysical, and radar-echo structure of a convective line with trailing stratiform precipitation viewed in a vertical cross section oriented perpendicular to the convective line (and generally parallel to its motion), as shown by the line AB in Figure 9.8. Intermediate and strong radar reflectivity is indicated by medium and dark shading. From Houze et al. (1989). Republished with permission of the American Meteorological Society.

The vorticity in the x - z plane ξ is governed by (2.51), which we write here as

$$\frac{D\xi}{Dt} + g \frac{\partial}{\partial x} \left(\frac{\theta^*}{\hat{\theta}} \right) = 0 \quad (9.3)$$

We may define a

$$(u, w) = (\psi_z, -\psi_x) \quad (9.4)$$

Then the vorticity, $\xi \equiv u_z - w_x$ [see (2.56)], becomes

$$\xi = \psi_{zz} + \psi_{xx} \quad (9.5)$$

Substituting (9.4) and (9.5) into (9.3) and applying the steady state assumption, we obtain

$$\psi_z \frac{\partial}{\partial x} (\psi_{zz} + \psi_{xx}) - \psi_x \frac{\partial}{\partial z} (\psi_{zz} + \psi_{xx}) + g \frac{\partial}{\partial x} \left(\frac{\theta^*}{\hat{\theta}} \right) = 0 \quad (9.6)$$

$$\xi = \frac{\partial u}{\partial z} - \frac{\partial w}{\partial x}$$

$$\frac{B}{g} \approx \frac{\theta'}{\theta} + 0.61q_v' - \frac{c_v p'}{c_p \bar{p}} - q_h$$

Quart. J. R. Met. Soc. (1972), **98**, pp. 336-352

551.511.6 : 551.515.41

The propagation and transfer properties of steady convective overturning in shear

By M. W. MONCRIEFF and J. S. A. GREEN
Imperial College, London

(Manuscript received 12 January 1971; in revised form 27 October 1971)

Quart. J. R. Met. Soc. (1981), **107**, pp. 29-50

551.511.62 : 551.558.1

A theory of organized steady convection and its transport properties

By M. W. MONCRIEFF
Atmospheric Physics Group, Imperial College, London

(Received 19 December 1979; revised 5 June 1980)

Quart. J. R. Met. Soc. (1978), **104**, 543-567

551.515.41 : 551.558.1

The dynamical structure of two-dimensional steady convection in constant vertical shear

By M. W. MONCRIEFF
Atmospheric Physics Group, Physics Department, Imperial College, London

(Received 25 July 1977; revised 14 November 1977)

Organized convective systems: Archetypal dynamical models, mass and momentum flux theory, and parametrization

By MITCHELL W. MONCRIEFF
National Center for Atmospheric Research, Boulder, Colorado 80307-3000, U.S.A.*

(Received 17 April 1991; revised 20 May 1992)

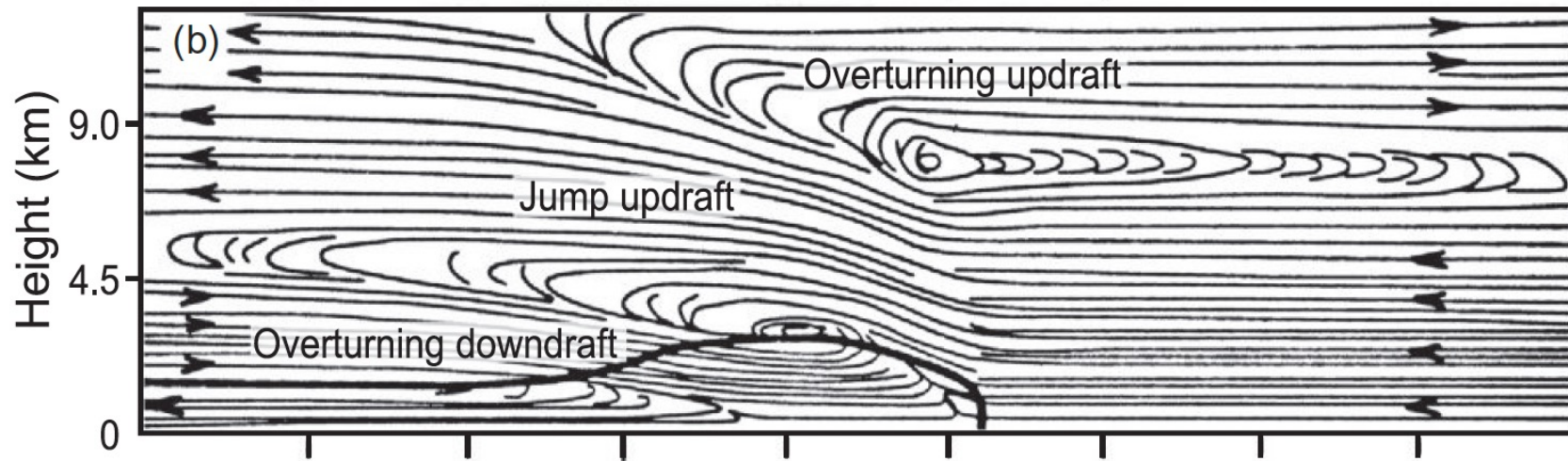


FIGURE 9.18 Time averaged numerical model simulation of a squall line with trailing stratiform precipitation. (a) Simulated radar reflectivity (in intervals of 5 dBZ). (b) Streamlines of system relative airflow. (c) Equivalent potential temperature (intervals of 3 K). Bold solid contour outlines cold pool (region of negative potential temperature perturbation). From Fovell and Ogura (1988). Republished with permission of the American Meteorological Society.

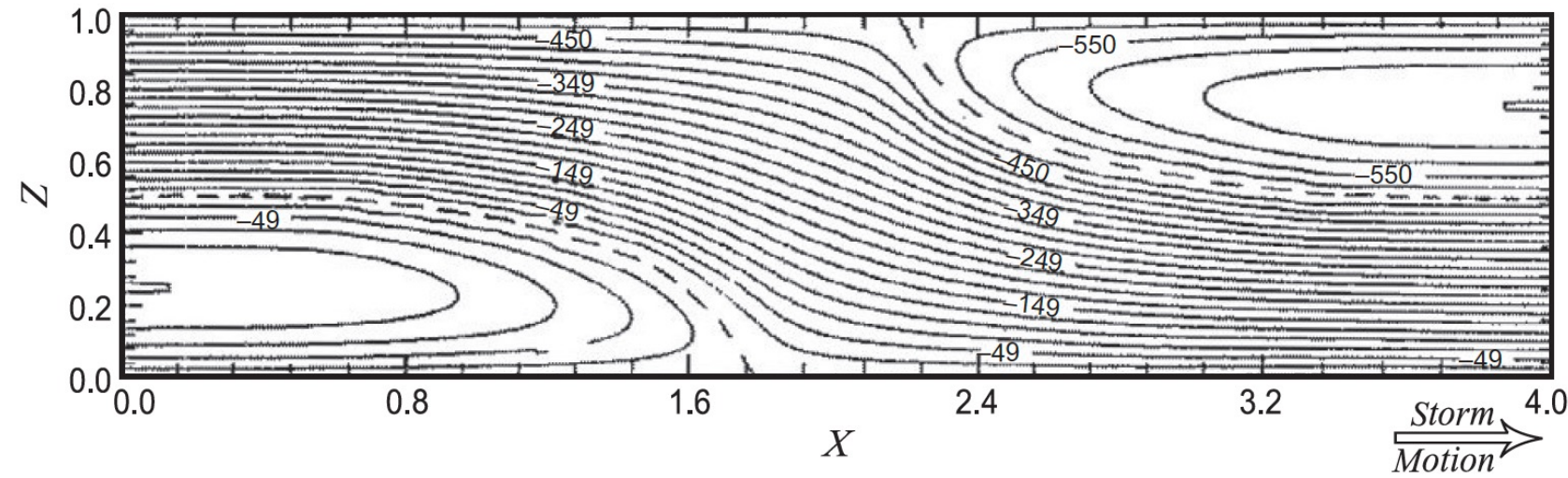


FIGURE 9.19 Two-dimensional relative stream function ψ calculated for the conditions of a squall-line MCS. Height z and horizontal distance x are in arbitrary units. From Moncrieff (1992). Republished with permission of the Royal Meteorological Society.

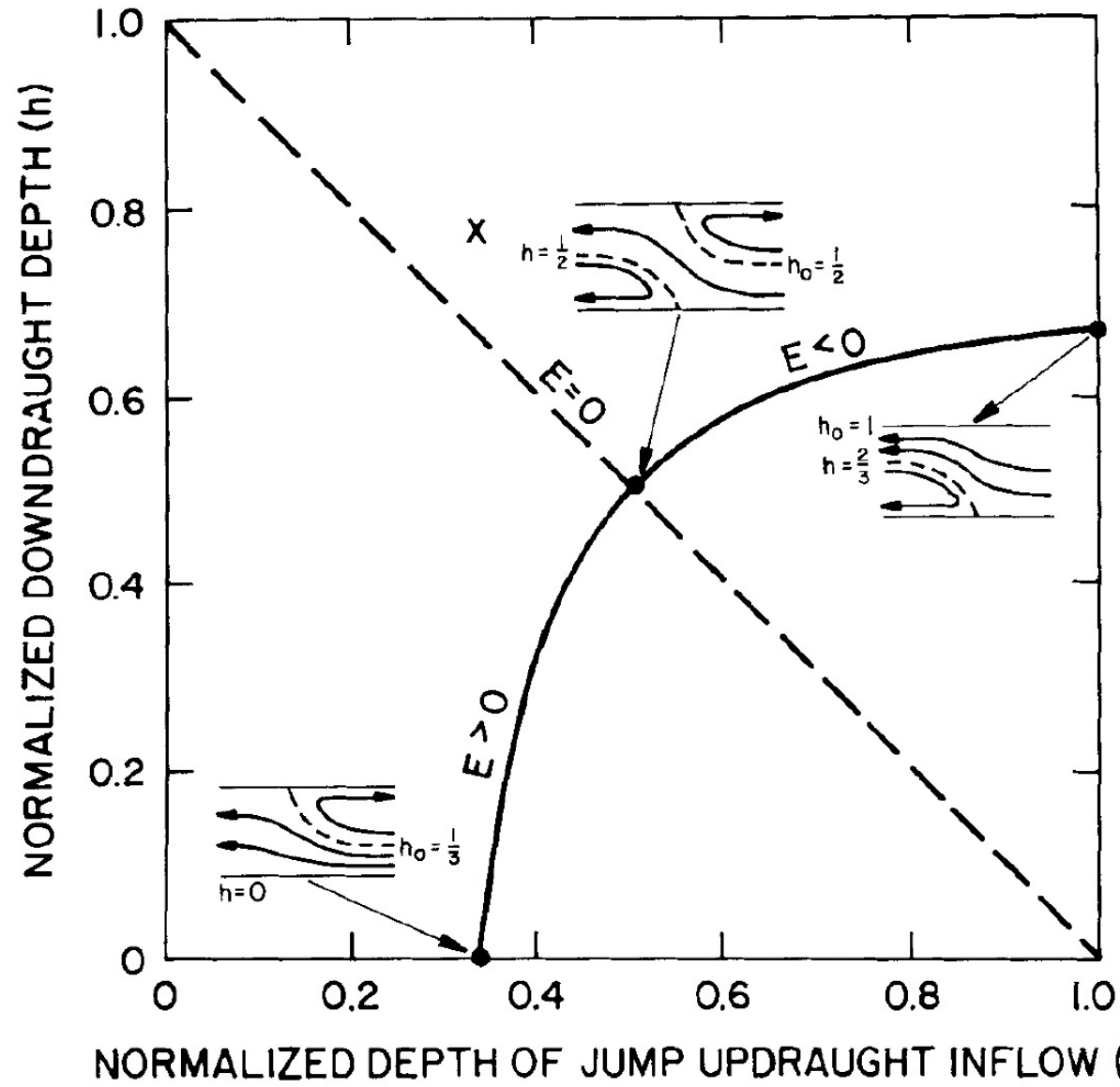


Figure 2. Solutions of the characteristic-regime equation showing the variation of the height of the downdraught, h , as a function of the inflow height of the jump, h_0 . Symmetric solutions shown by the broken line and asymmetric solutions by the full line. Inlaid diagrams show flow organization for limiting cases $h = 0$, $h = \frac{1}{2}$ and $h = \frac{2}{3}$ corresponding to $E = \frac{8}{9}$, 0 and -8 , respectively. X marks the sheared inflow solution obtained in section 5(d).

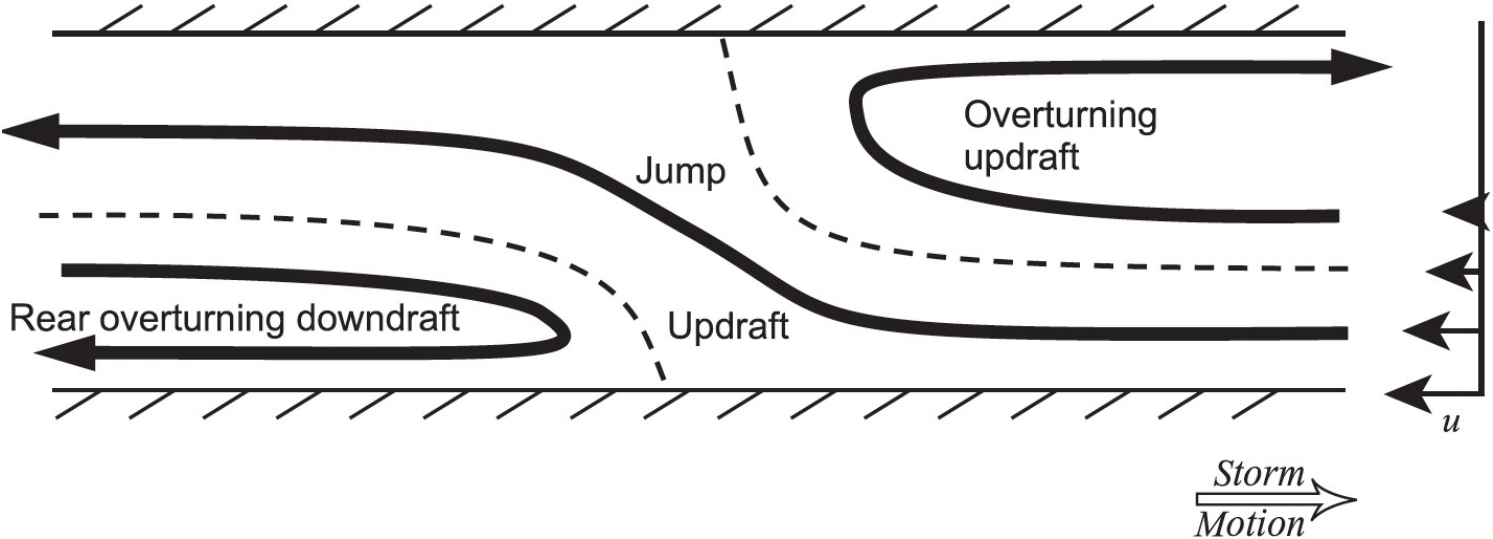


FIGURE 9.20 Schematic diagram of the airflow in a squall-line MCS occurring in an environment with low-level shear, as indicated on the right-hand side. The flow consists of three characteristic branches: the jump updraft, the rear overturning downdraft, and the overturning updraft. Adapted from Moncrieff (1992). Republished with permission of the Royal Meteorological Society.

Consider a steady solution with all variable u only depending on ψ and z

$$u = u(\psi(x, z), z)$$

3D momentum equations reads as follows

$$\frac{D\mathbf{v}}{Dt} = -\frac{1}{\rho_o} \nabla p^* - f \mathbf{k} \times \mathbf{v} + B \mathbf{k} + \mathbf{F} \quad (2.47)$$

Making Boussinesq assumption $\rho_o = \text{const.}$

$$wB = \frac{D}{Dt} \int_{z_{in}}^z B(\psi, z') dz'$$

Taking $\mathbf{v} \cdot (2.47)$, making the Boussinesq assumption, ignoring friction, and using the identity (9.9), we obtain the Bernoulli equation

$$\frac{1}{2}(u^2 + w^2) + \frac{p^*}{\rho_o} - \int_{z_{in}}^{z(t)} g \left(\frac{\theta^*}{\hat{\theta}} \right) dz = \text{constant on streamline}$$

中尺度对流复合体的流场

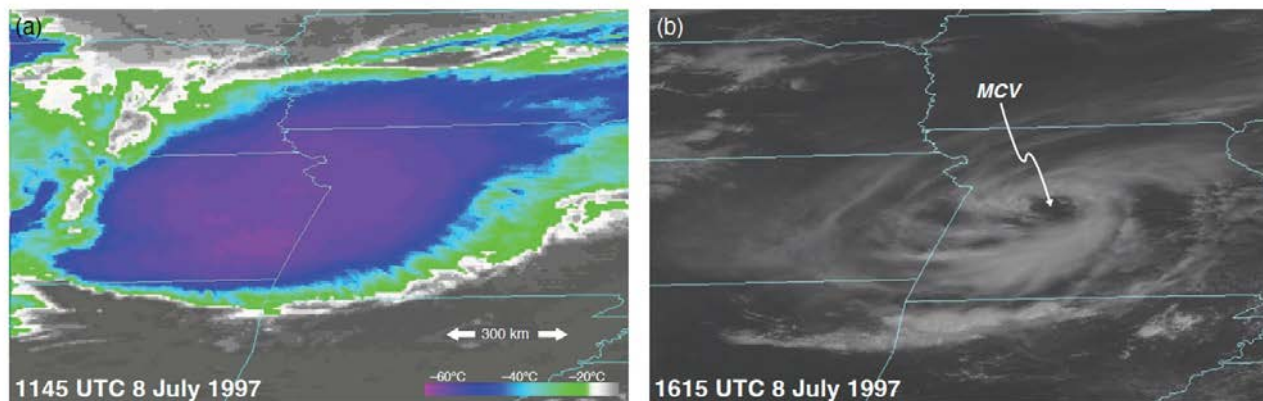


Figure 9.30 (a) Infrared satellite image of a weakening MCC at 1145 UTC 8 July 1997. (b) Visible satellite image of an MCV at 1615 UTC 8 July 1997. The circulation was produced by the MCC in (a).

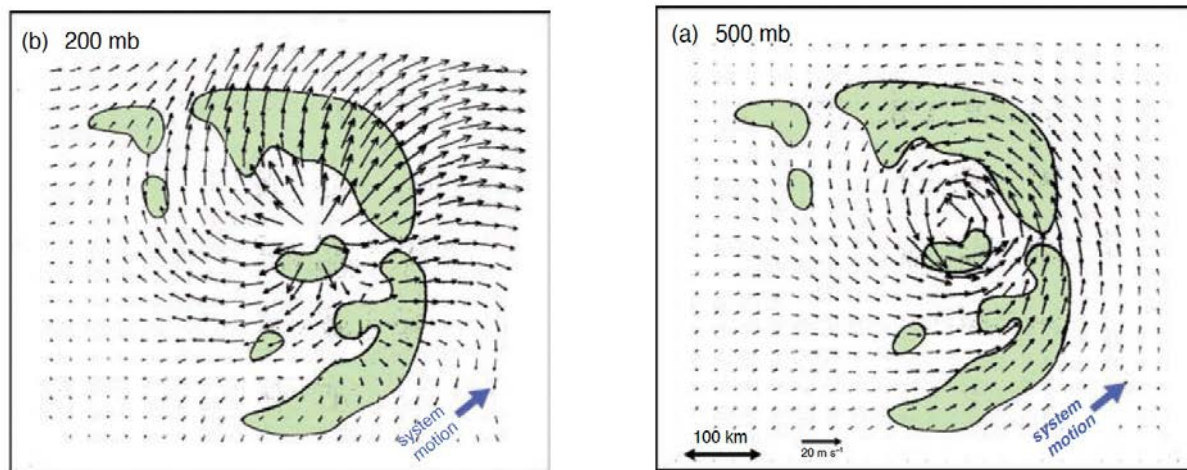
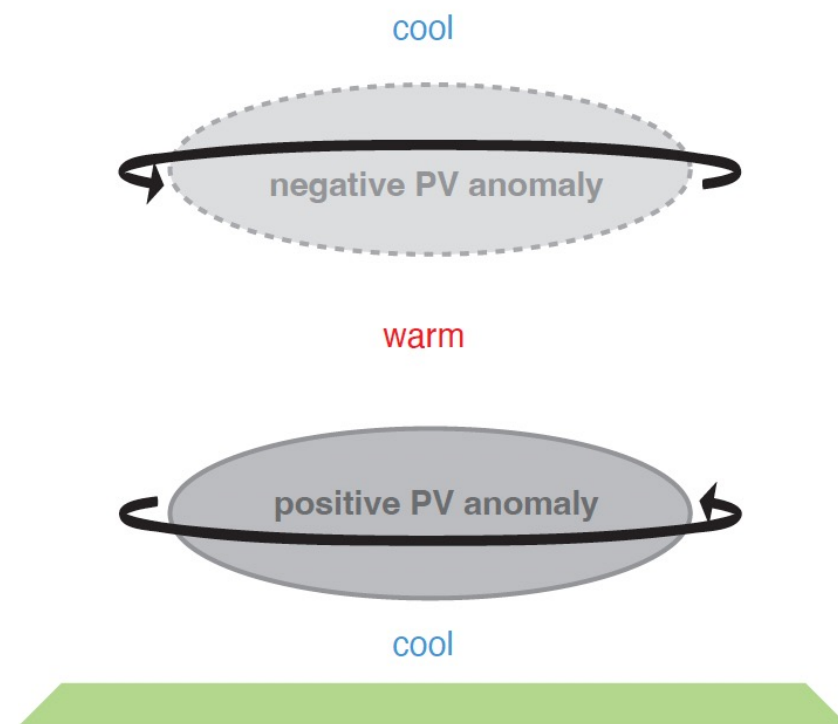


Figure 9.29 Mesoscale model output showing cyclonic vorticity at 500 mb and anticyclonic vorticity at 200 mb in the wake of a midlatitude mesoscale convective complex. Winds are system-relative. Green shading denotes regions of convective precipitation. (Adapted from Chen and Frank [1993].)



Ertel PV theorem

$$\frac{d}{dt} \left\{ \frac{\boldsymbol{\omega}_a \cdot \nabla \lambda}{\rho} \right\} = \frac{\boldsymbol{\omega}_a}{\rho} \cdot \nabla \Psi + \nabla \lambda \cdot \left[\frac{\nabla \rho \times \nabla p}{\rho^3} \right] + \frac{\nabla \lambda}{\rho} \cdot \left\{ \nabla \times \frac{\mathcal{F}}{\rho} \right\}.$$

Geophysical Fluid Dynamics by Pedlosky (1986)

The derivation begins with the hydrostatic primitive equations with minor approximation in the thermodynamic terms

$$d\mathbf{v}/dt + \theta_0 \nabla \pi' + f \mathbf{k} \times \mathbf{v} = \mathbf{F}, \quad (1)$$

$$\theta_0 (\partial \pi' / \partial z) - b' = 0, \quad (2)$$

$$\nabla \cdot \mathbf{v} + \rho_0^{-1} (\partial \rho_0 w / \partial z) = 0, \quad (3)$$

$$db'/dt + N^2 w = gH/\theta_0, \quad (4)$$

$$u = -\frac{\partial \psi}{\partial y} \quad v = \frac{\partial \psi}{\partial x}$$

To the extent that vertical velocities are small, ϕ can be ignored, and the x and y components of vorticity can be approximated as

见板书!
$$\zeta_x \approx -\partial^2 \psi / \partial x \partial z, \quad \zeta_y \approx -\partial^2 \psi / \partial y \partial z. \quad (10)$$

The potential vorticity $q = \rho^{-1} (\boldsymbol{\zeta} + f \mathbf{k}) \cdot \nabla \theta$ thus becomes, to this degree of approximation,

$$q = \frac{1}{\rho_0} \left[-\frac{\partial^2 \psi}{\partial x \partial z} \frac{\partial \theta}{\partial x} - \frac{\partial^2 \psi}{\partial y \partial z} \frac{\partial \theta}{\partial y} + (f + \nabla^2 \psi) \frac{\partial \theta}{\partial z} \right], \quad (11)$$

Raymond and Jiang (1990)

Any difference from QG theory?

$$\frac{g \rho_0 q'}{\theta_0} = \frac{f}{\theta_0} \frac{\partial}{\partial z} \left(\theta_0^2 \frac{\partial \pi'}{\partial z} \right) + N^2 \nabla^2 \psi - \theta_0 \left(\frac{\partial^2 \psi}{\partial x \partial z} \frac{\partial^2 \pi'}{\partial x \partial z} + \frac{\partial^2 \psi}{\partial y \partial z} \frac{\partial^2 \pi'}{\partial y \partial z} \right). \quad (12)$$

$$\nabla^2 (\theta_0 \pi' - f \psi) = 2 \frac{\partial^2 \psi}{\partial x^2} \frac{\partial^2 \psi}{\partial y^2} - 2 \left(\frac{\partial^2 \psi}{\partial x \partial y} \right)^2. \quad (13)$$

请参考 Raymond and Jiang (1990)

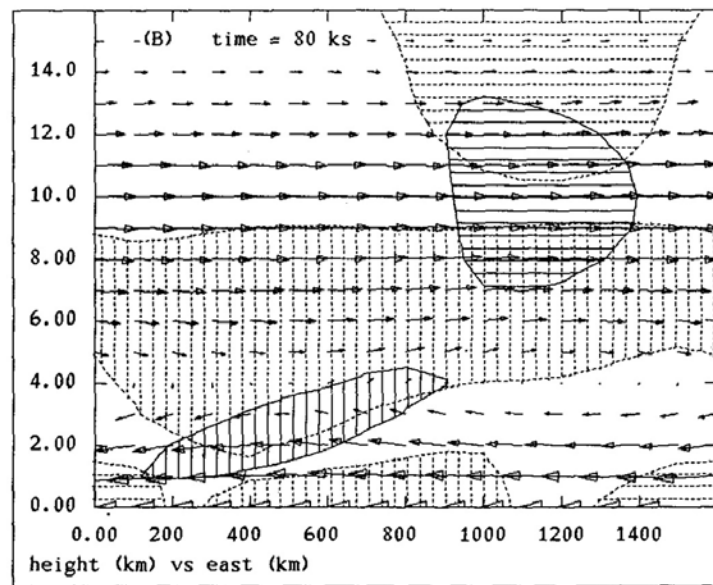
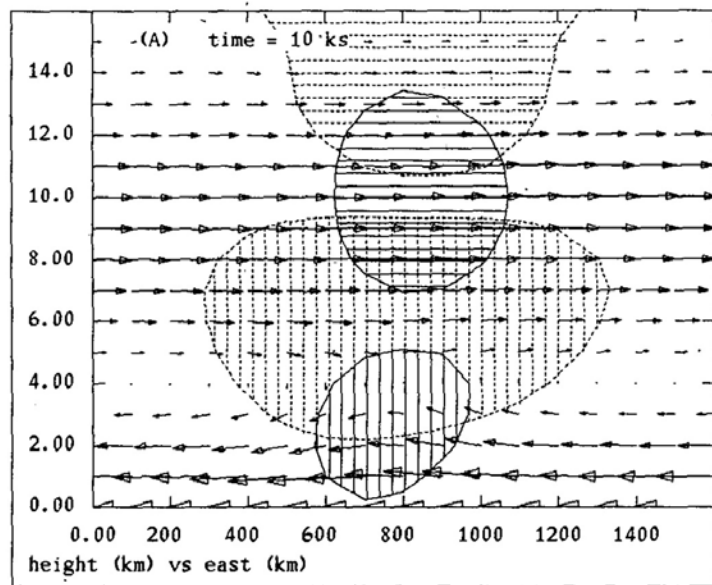


FIG. 5. Potential vorticity, temperature anomalies, and flow in a vertical east-west plane at $y = 800$ km. Solid vertical hatching indicates where the lower potential vorticity anomaly has $\eta' > 0.1$ pvu. The upper anomaly is indicated by solid horizontal hatching, which indicates regions with $\eta' < -0.3$ pvu. Broken hatching shows potential temperature anomalies greater than $\pm 0.5^\circ\text{K}$ with vertical hatching indicating warm regions and horizontal hatching indicating cool regions. Wind vector scale is $0.05 \text{ m s}^{-1} \text{ km}^{-1}$. Thus, a wind vector with a horizontal component of 100 km corresponds to 5 m s^{-1} , whereas a vertical component 1 km long corresponds to 5 cm s^{-1} . (a) At time = 10 ks. (b) At time = 80 ks.

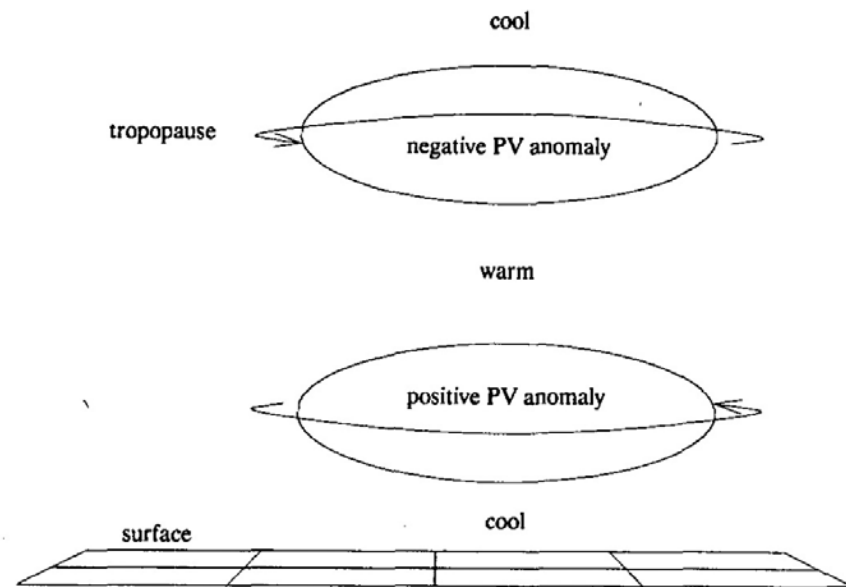


FIG. 1. Postulated structure of potential vorticity anomalies produced by a region of convection and the associated changes in temperature and wind structure. The circulation is cyclonic around the lower, positive anomaly, and anticyclonic around the upper anomaly as shown by the arrows.

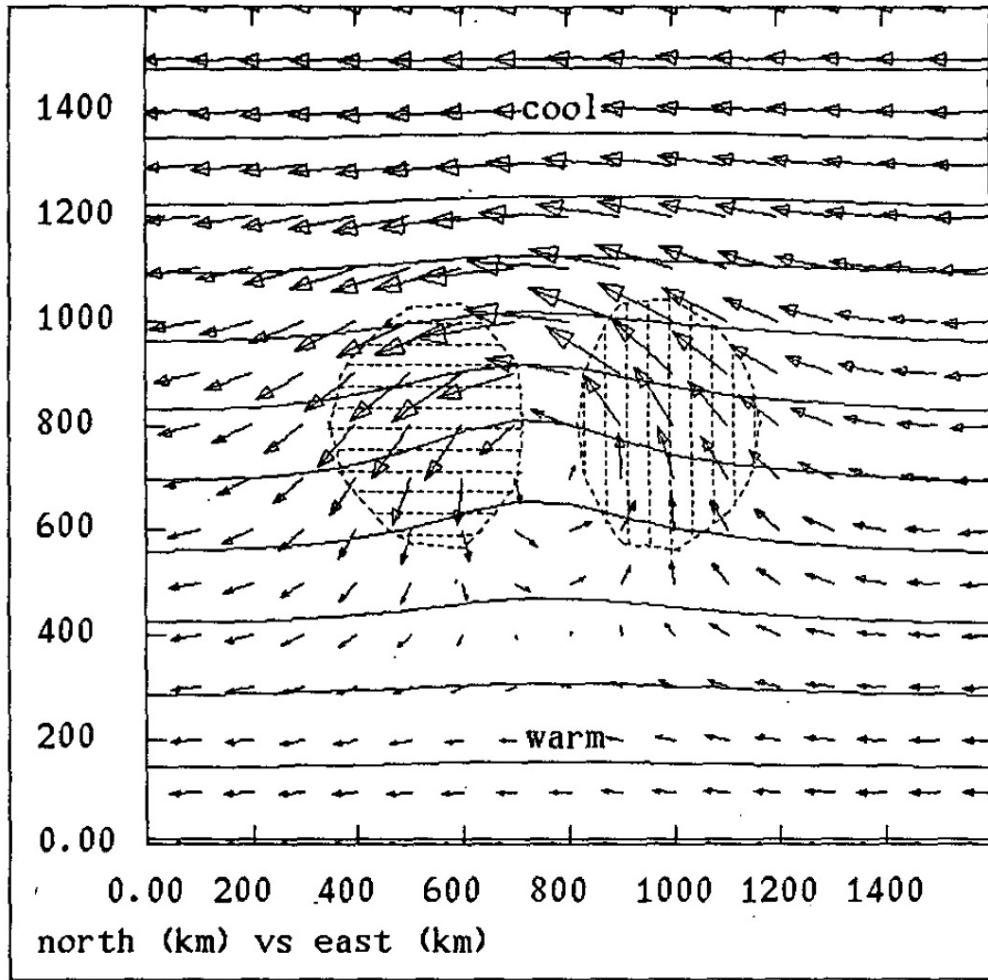


FIG. 6. Flow and potential temperature at $z = 3$ km and $t = 10$ ks. Contours indicate constant values of potential temperature at 1°K intervals, with cooler regions to the north. Vectors show the horizontal flow with a scale of 3 m s^{-1} per 100 km. Vertical hatching shows updrafts in excess of 0.5 cm s^{-1} , while downdrafts less than -0.5 cm s^{-1} are indicated by horizontal hatching.

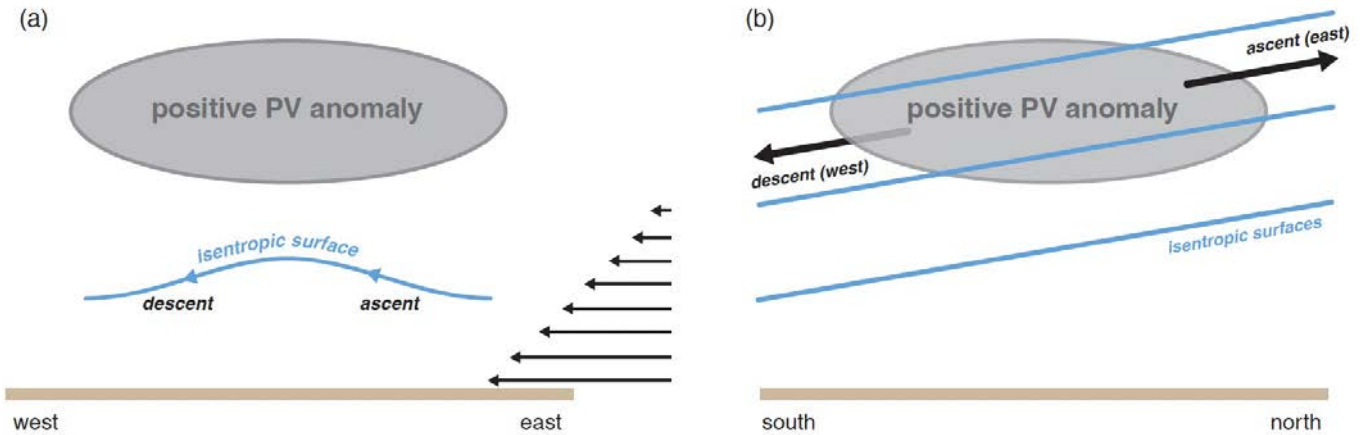
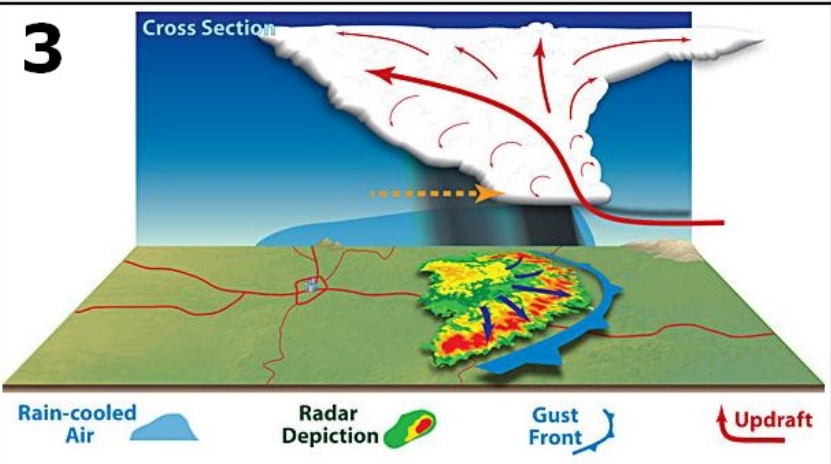
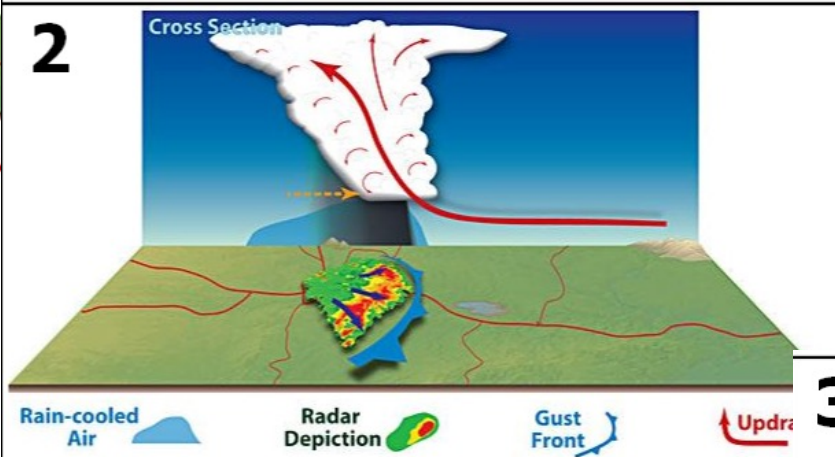
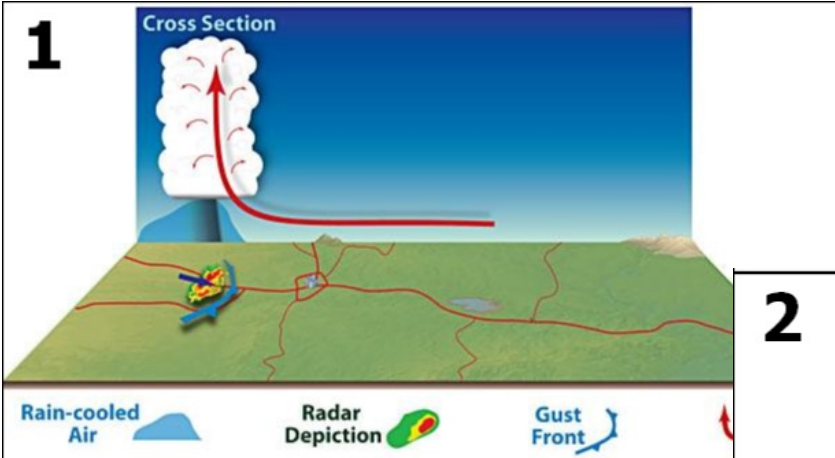


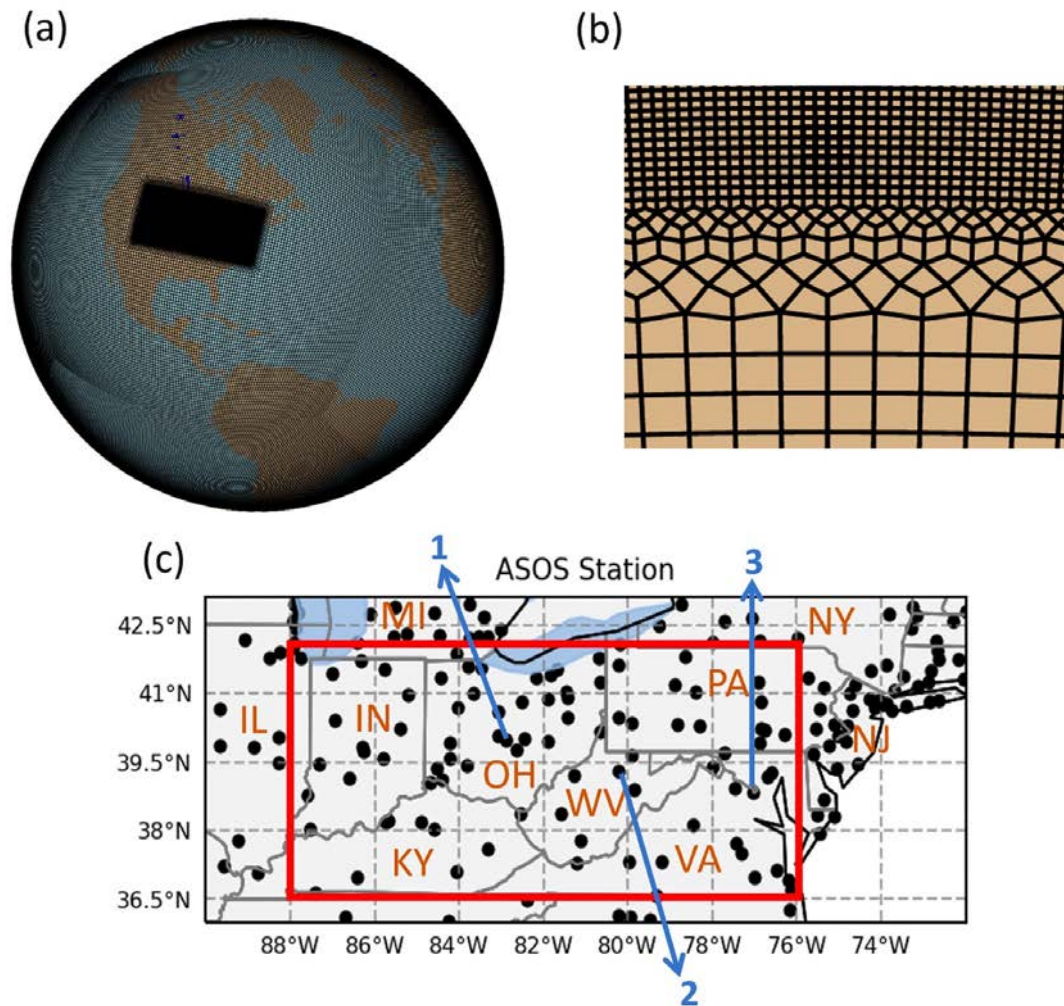
Figure 9.34 Illustrations of the mechanisms by which ascent can occur in the presence of a potential vorticity anomaly in shear. The environmental shear is westerly in the illustration and only shown below the positive potential vorticity anomaly for clarity. (a) In a frame of reference moving with the potential vorticity anomaly, the relative environmental wind causes flow on the perturbation isentropic surface caused by the potential vorticity anomaly, with ascent (descent) upwind (downwind) of the anomaly. (b) The potential vorticity anomaly, as viewed from the east. The tilted isentropic surfaces are associated with the environmental westerly wind shear indicated in (a). The cyclonic circulation around the potential vorticity anomaly causes ascent (descent) in the southerlies (northerlies) east (west) of the anomaly. (Adapted from Raymond and Jiang [1990].)

强对流风暴 (derecho)



来自wikipedia

强对流风暴 (derecho) 的模拟



The June 2012 North American Derecho: A Testbed for Evaluating Regional and Global Climate Modeling Systems at Cloud-Resolving Scales

W. Liu¹, P. A. Ullrich¹, J. Li², C. Zarzycki³, P. M. Caldwell⁴, L. R. Leung², and Y. Qian²

¹Department of Land, Air, and Water Resources, University of California-Davis, Davis, CA, USA, ²Pacific Northwest National Laboratory, Richland, WA, USA, ³Department of Meteorology and Atmospheric Science, Pennsylvania State University, University Park, PA, USA, ⁴Lawrence Livermore National Lab, Livermore, CA, USA

Figure 1. (a) The SCREAM regionally refined model (RRM) grid, shown using a global orthographic projection. (b) The transition region in the RRM grid from LR to HR resolution. (c) Locations of Automated Surface Observation System stations in black circles. The red box shows the analysis region (76°–88°W, 36.5°–42°N).

Table 1*A Summary of the SCREAM Regionally Refined Model Simulations Conducted and Compared in This Study*

Simulation abbreviation	Fine resolution	IC	Initialization time (UTC)	LR/HR configuration	Dynamical core
SCREAM_6.5 km	ne512 (6.5 km)	ERA5+RAP	12:00 29 June 2012	HR	NH
SCREAM_3.25 km	ne1024 (3.25 km)	ERA5+RAP	12:00 29 June 2012	HR	NH
SCREAM_1.625 km	ne2048 (1.625 km)	ERA5+RAP	12:00 29 June 2012	HR	NH
SCREAM_ERA5	ne1024 (3.25 km)	ERA5	12:00 29 June 2012	HR	NH
SCREAM_ERAI	ne1024 (3.25 km)	ERA5	12:00 29 June 2012	HR	NH
SCREAM_06Z	ne1024 (3.25 km)	ERA5+RAP	06:00 29 June 2012	HR	NH
SCREAM_LR	ne1024 (3.25 km)	ERA5+RAP	12:00 29 June 2012	LR	NH
SCREAM_H	ne1024 (3.25 km)	ERA5+RAP	12:00 29 June 2012	HR	H

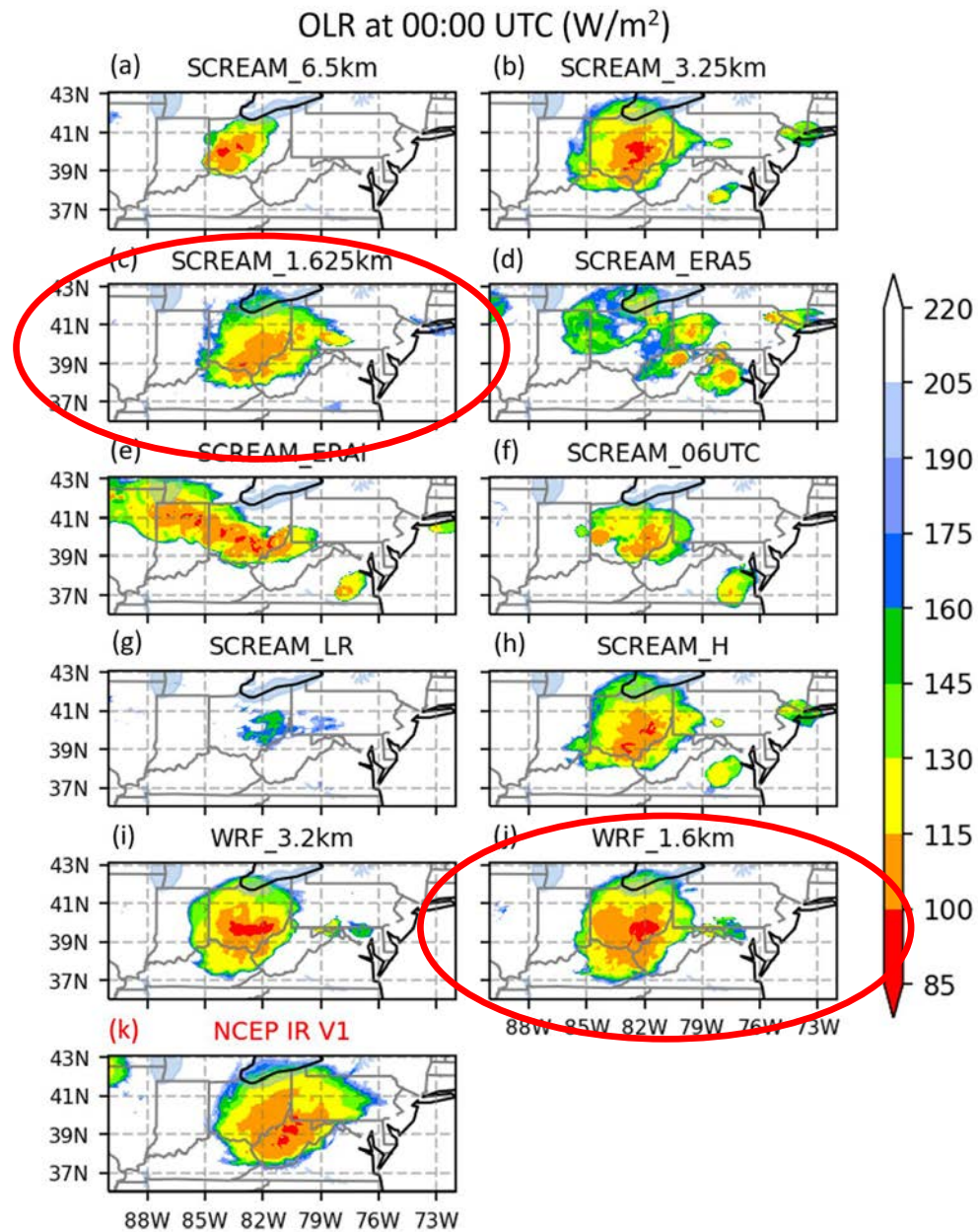


Figure 2. Outgoing longwave radiation (W/m^2) at 00:00 UTC 30 June 2012 in (a) SCREAM_6.5 km, (b) SCREAM_3.25 km, (c) SCREAM_1.625 km, (d) SCREAM_ERA5, (e) SCREAM_ERAI, (f) SCREAM_06UTC, (g) SCREAM_LR, (h) SCREAM_H, (i) WRF_3.2 km, (j) WRF_1.6 km, and (k) NCEP IR V1. All datasets are remapped to 0.05° resolution. The panel with red title denotes the reference data set.

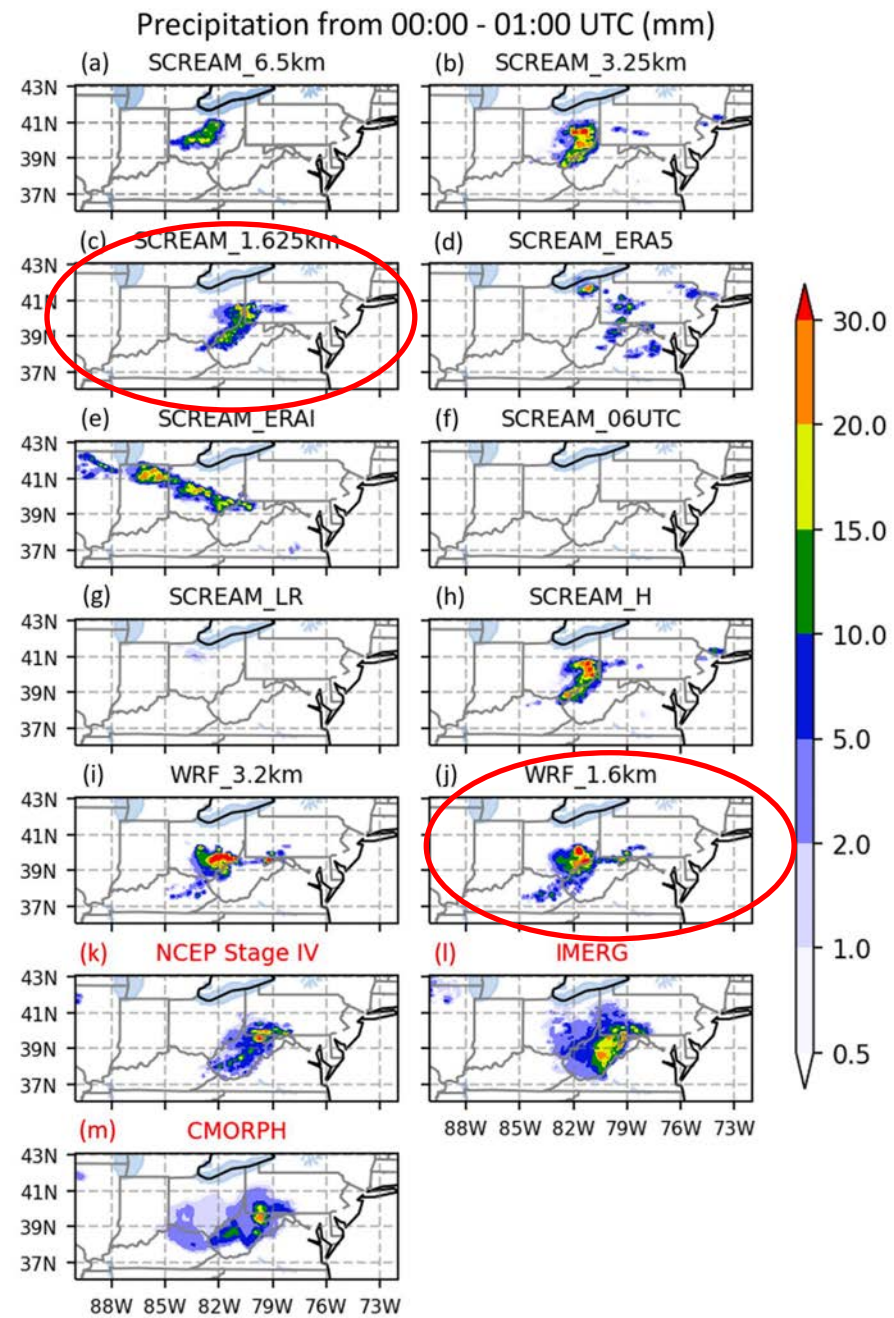


Figure 4. Same as Figure 2 but for accumulated precipitation (mm) from 00:00 - 01:00 UTC 30 June 2012. Panels (k-m) show NCEP Stage IV, IMERG, and CMORPH precipitation, respectively. All datasets are remapped to 0.1°.

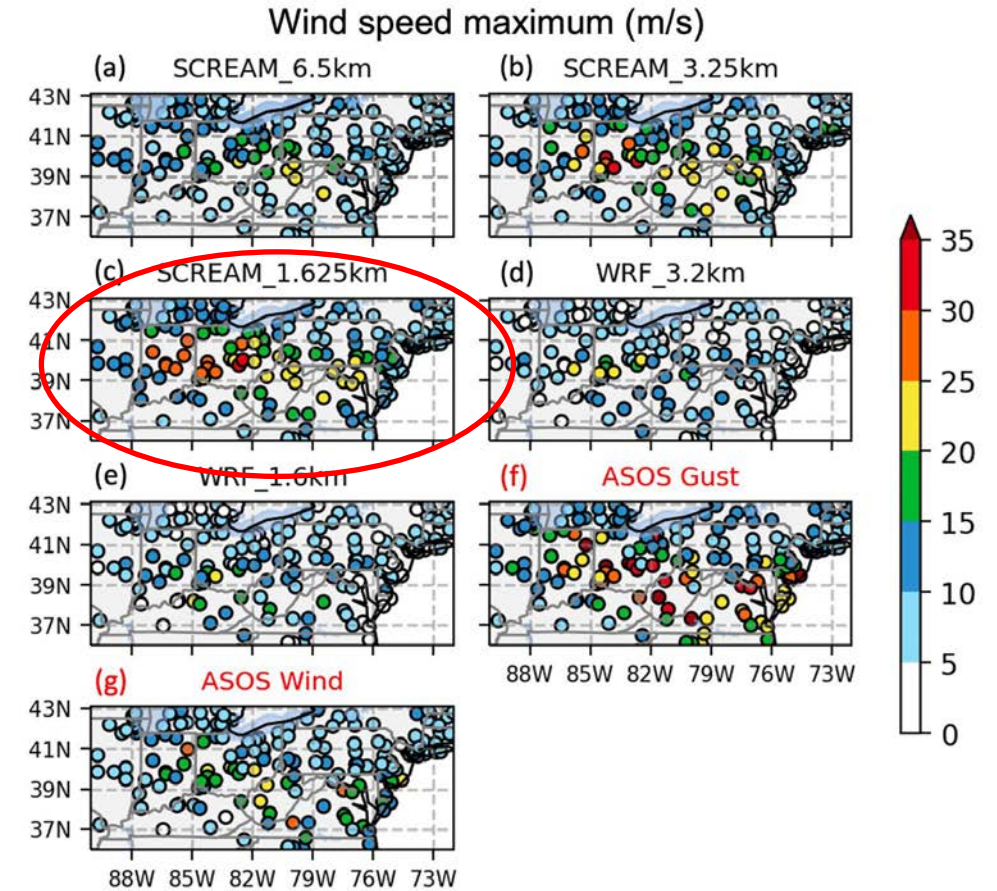
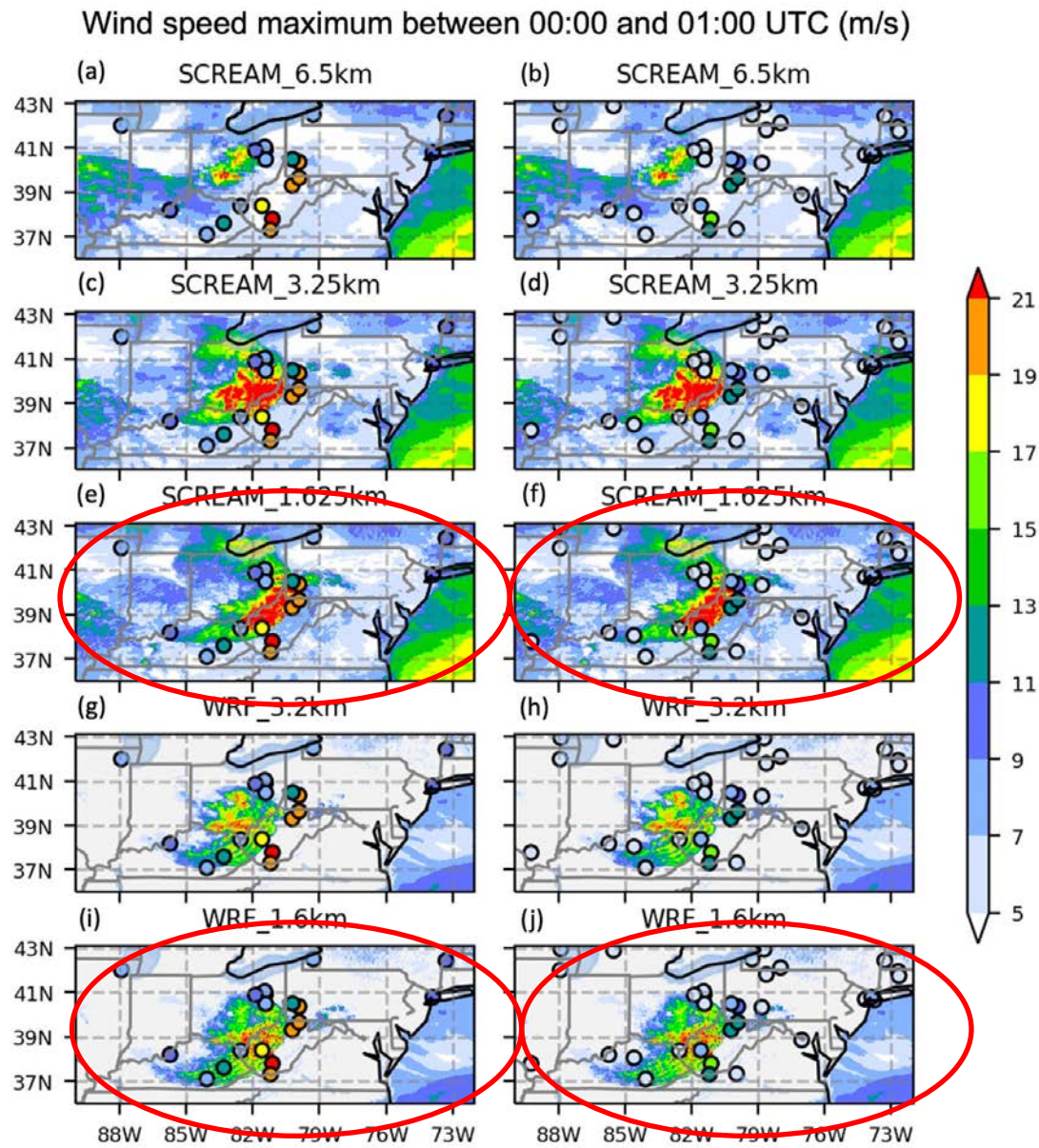


Figure 12. Wind speed maximum (m/s) between 18:00 UTC 29 June and 06:00 UTC 30 June 2012 in (a) SCREAM_6.5 km, (b) SCREAM_3.25 km, (c) SCREAM_1.625 km, (d) WRF_3.2 km, (e) WRF_1.6 km, (f) Automated Surface Observation System (ASOS) gust, and (g) ASOS wind. Only ASOS sites with gust reports during the period are displayed. Panels (a–e) show results at the closest grid points to the ASOS locations.

Figure 5. Wind speed maximum (m/s; shaded) between 00:00 and 01:00 UTC 30 June 2012 in (a, b) SCREAM_6.5 km, (c, d) SCREAM_3.25 km, (e, f) SCREAM_1.625 km, (g, h) WRF_3.2 km, and (i, j) WRF_1.6 km. The dot markers represent the Automated Surface Observation System (ASOS) gust wind speed maximum (m/s) in the left panels and wind speed maximum (m/s) in the right panels. The ASOS stations with wind speed maximum lower than 5 m/s are not shown in the right panels. All simulation results are displayed at raw grids.

Challenges in Numerical Weather Prediction of the 10 August 2020 Midwestern Derecho: Examples from the FV3-LAM

WILLIAM A. GALLUS JR. ^a AND MICHELLE A. HARROLD ^b

^a Department of Geological and Atmospheric Sciences, Iowa State University, Ames, Iowa

^b National Center for Atmospheric Research/Research Applications Laboratory and Developmental Testbed Center, Boulder, Colorado

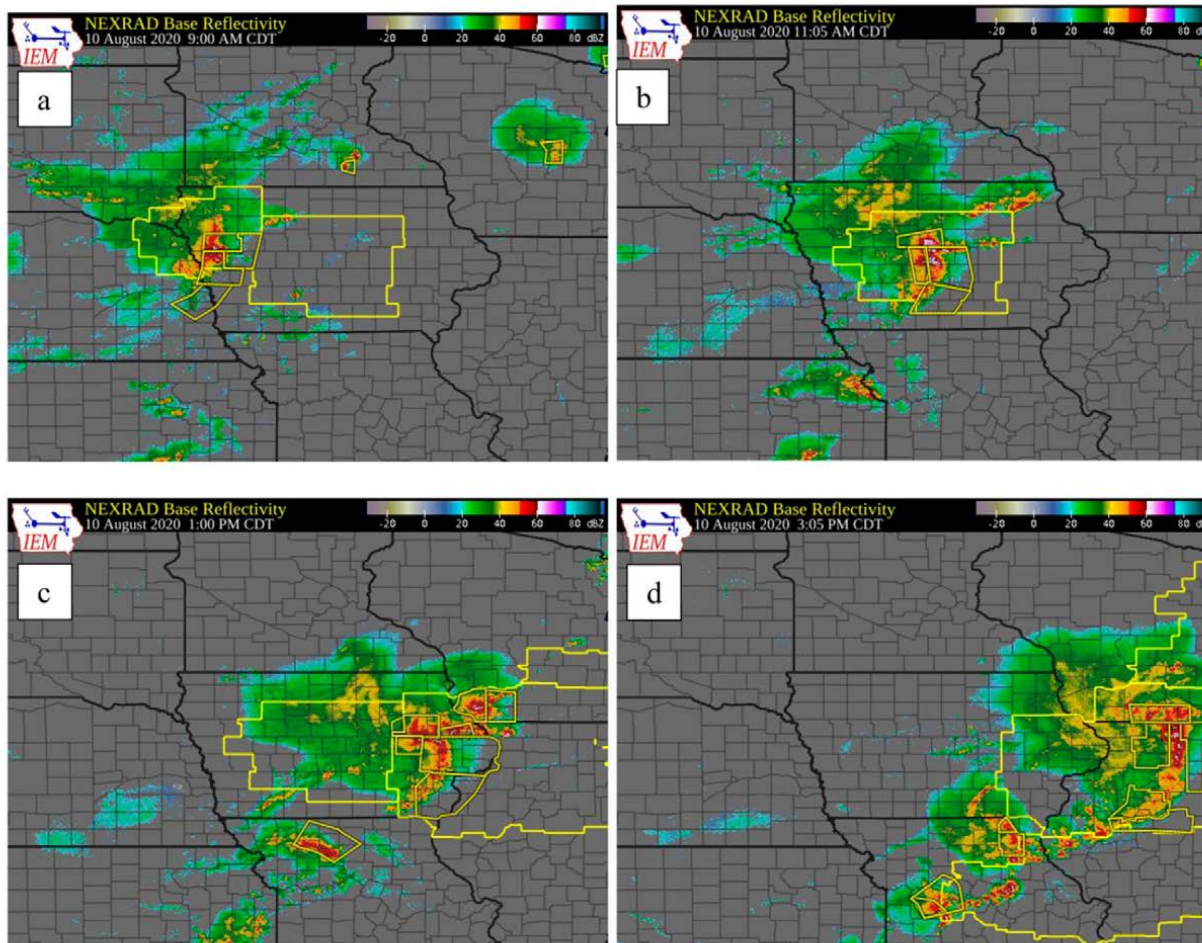


FIG. 1. Composite NEXRAD reflectivity at (a) 1400, (b) 1600, (c) 1800, and (d) 2000 UTC 10 Aug 2020. Severe thunderstorm warnings are overlaid with thin yellow lines. Severe thunderstorm watches are indicated with thicker yellow lines. The images are from the Iowa Environmental Mesonet.

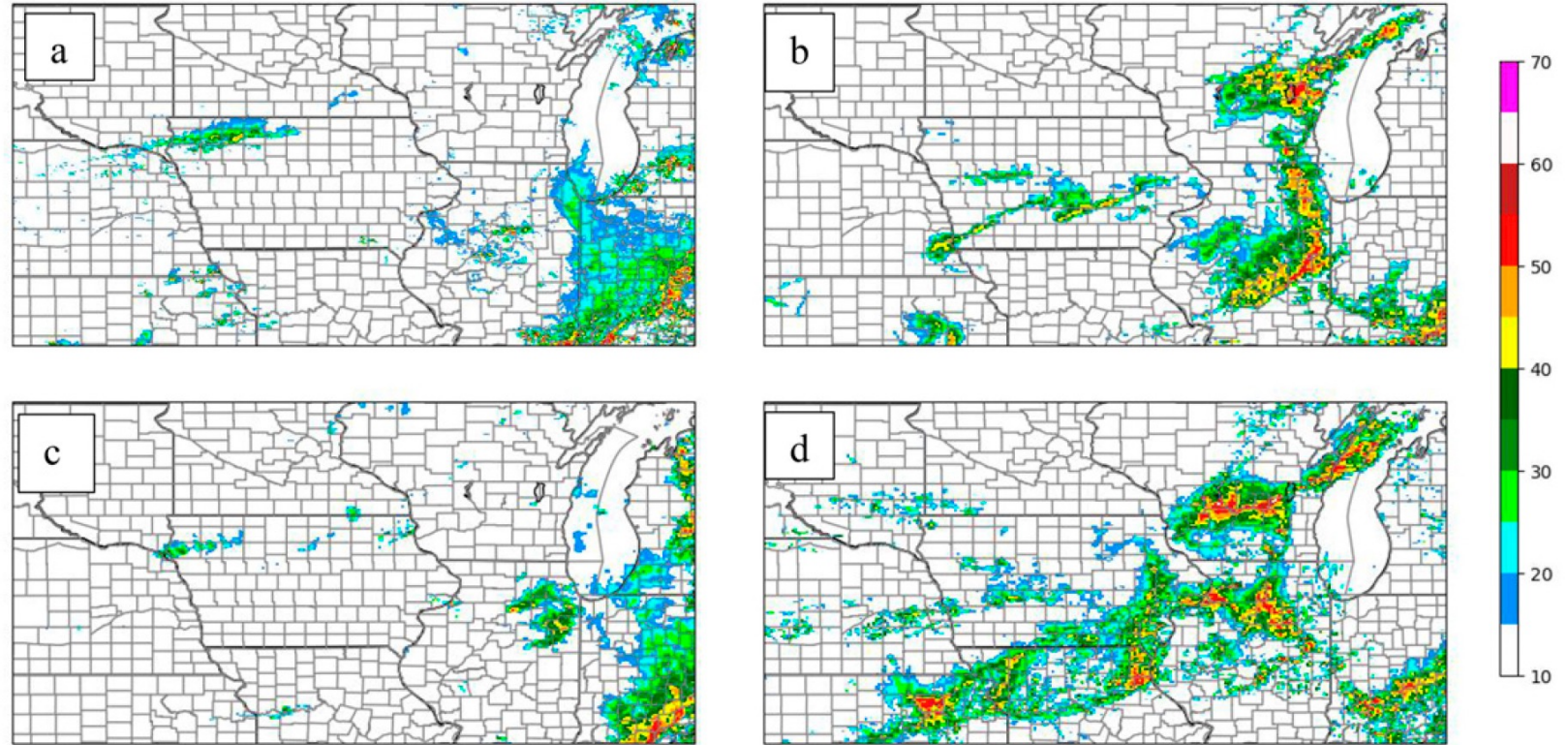
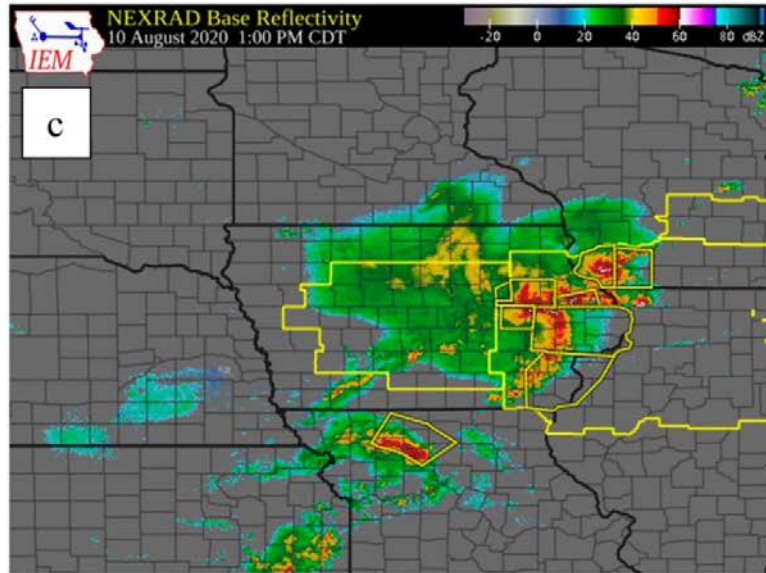
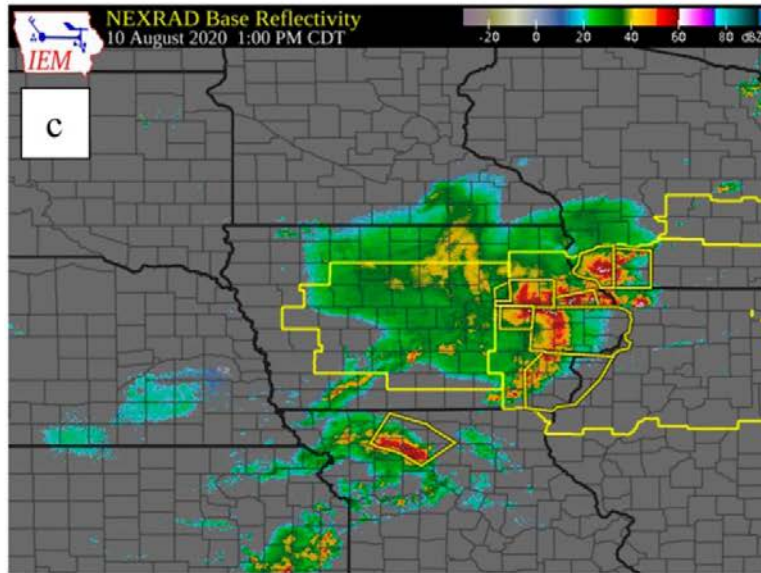
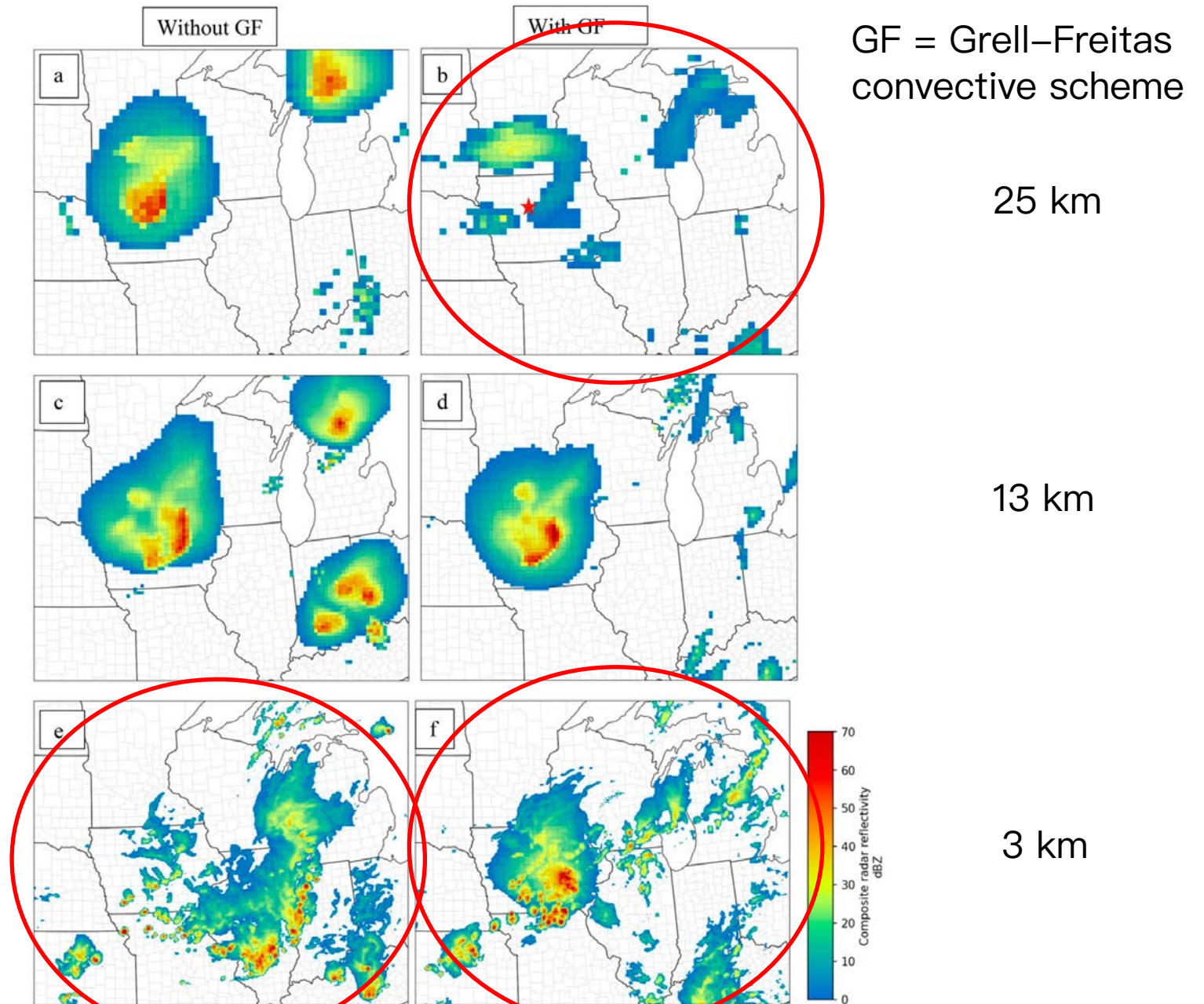


FIG. 4. Simulated composite reflectivity valid at 1800 UTC 10 Aug 2020 from four HREF members initialized at 0000 UTC 10 Aug 2020, with (a) 3-km North American Model Nest (Rogers et al. 2017), (b) High Resolution Window Advanced Research version of the Weather Research and Forecasting (WRF) Model (Skamarock et al. 2008), (c) CONUS Member 2 (formerly known as the National Severe Storms Laboratory WRF; Kain et al. 2010), and (d) High Resolution Window NMMB (Janjić and Gall 2012).

The limited Area Model (LAM) version of the Finite-Volume-Cubed-Sphere atmospheric dynamical core (FV3-LAM)



Three unusual behaviors!



GF = Grell-Freitas convective scheme

25 km

13 km

3 km

FIG. 5. Simulated reflectivity (see color bar at right) at 1800 UTC for the RRFs runs initialized at 0000 UTC 10 Aug 2020 for (a) 25 km without GF, (b) 25 km with GF, (c) 13 km without GF, (d) 13 km with GF, (e) 3 km without GF, and (f) 3 km with GF. The observed radar valid at this time can be found in Fig. 1b. The red star in (b) shows where the sounding is taken from in Fig. 9.

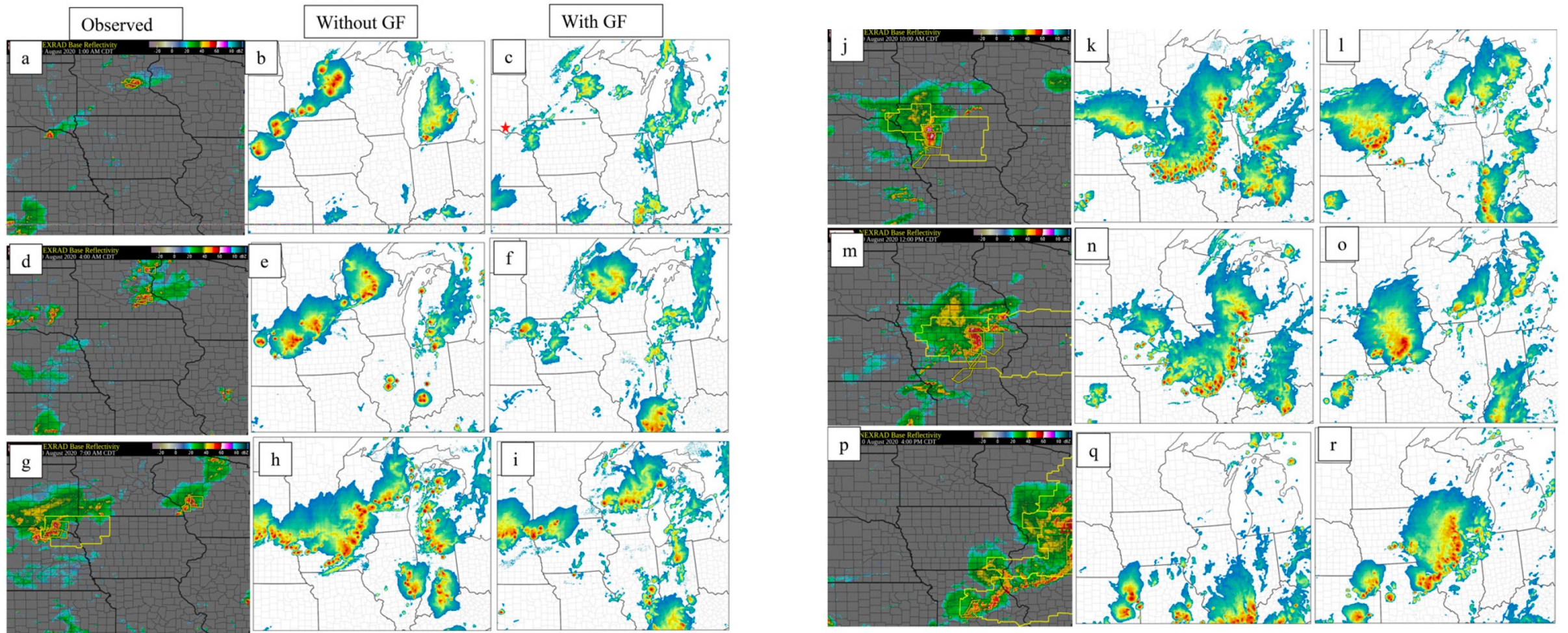
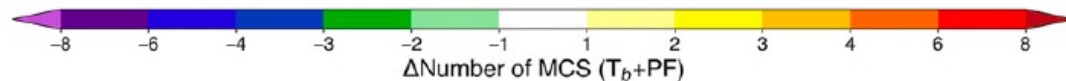
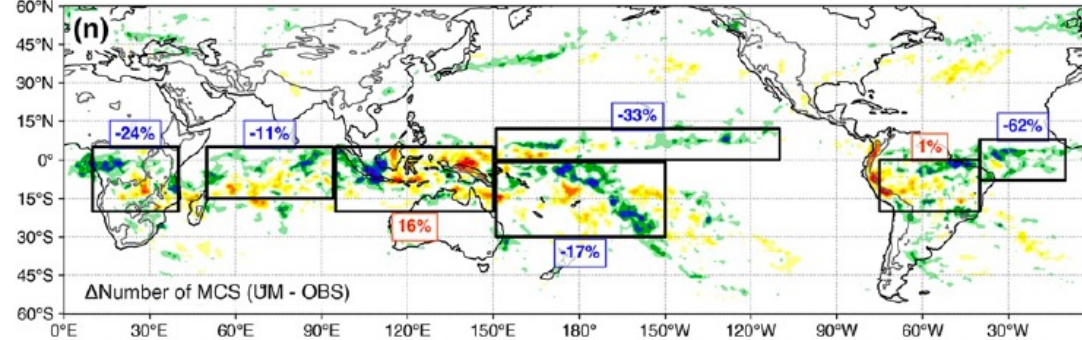
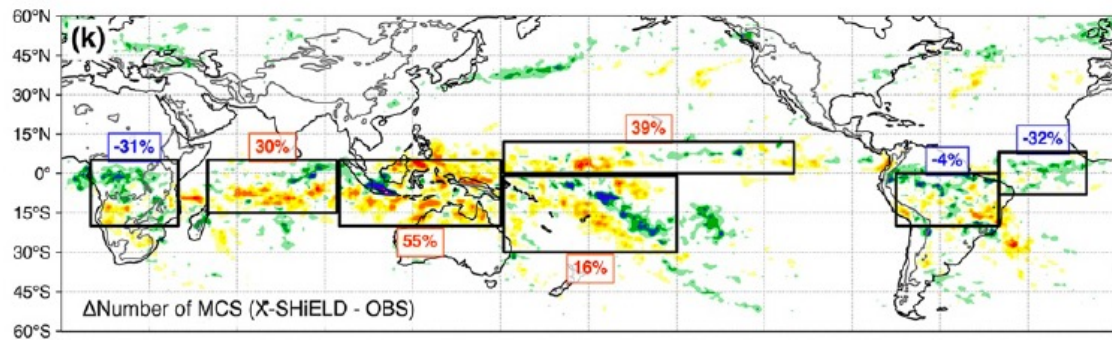
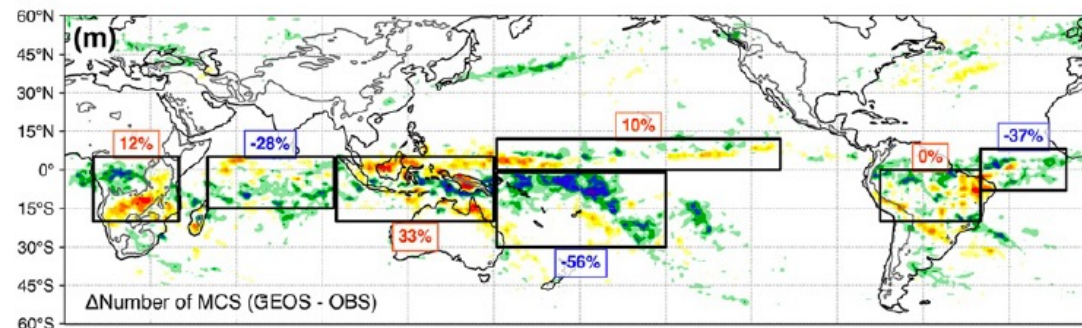
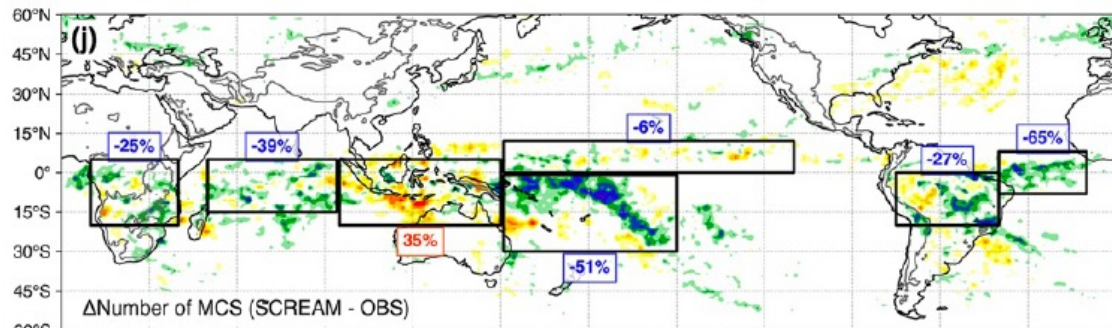
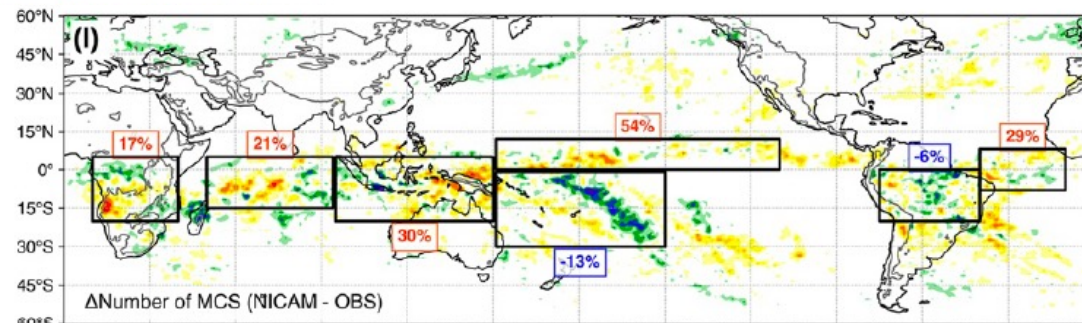
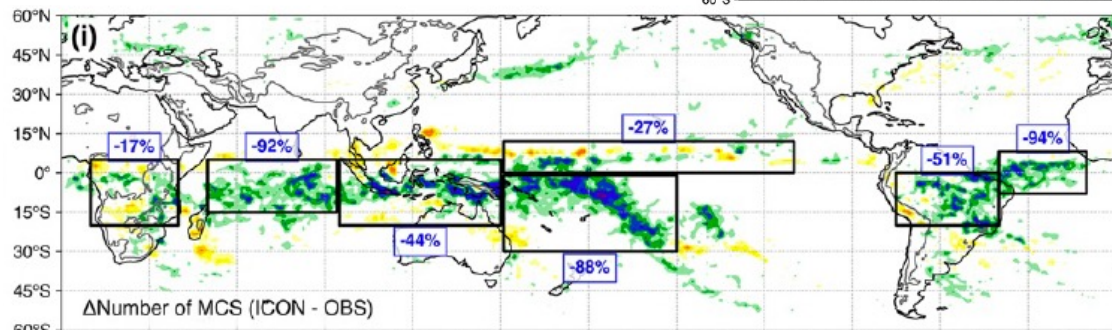
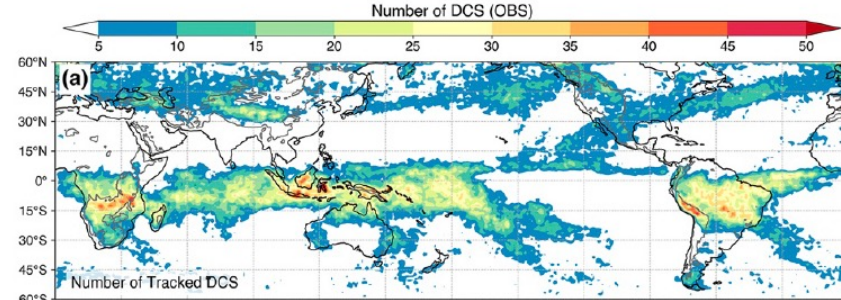


FIG. 10. (left) Observed reflectivity, and simulated reflectivity from (center) the 3-km RRFS run without the GF scheme and (right) the RRFS run with the GF scheme at (a)–(c) 0600, (d)–(f) 0900, (g)–(i) 1200, (j)–(l) 1500, (m)–(o) 1700, and (p)–(r) 2100 UTC. The red star in (c) indicates where the sounding used in Fig. 13 is taken.

模拟MCS统计特征



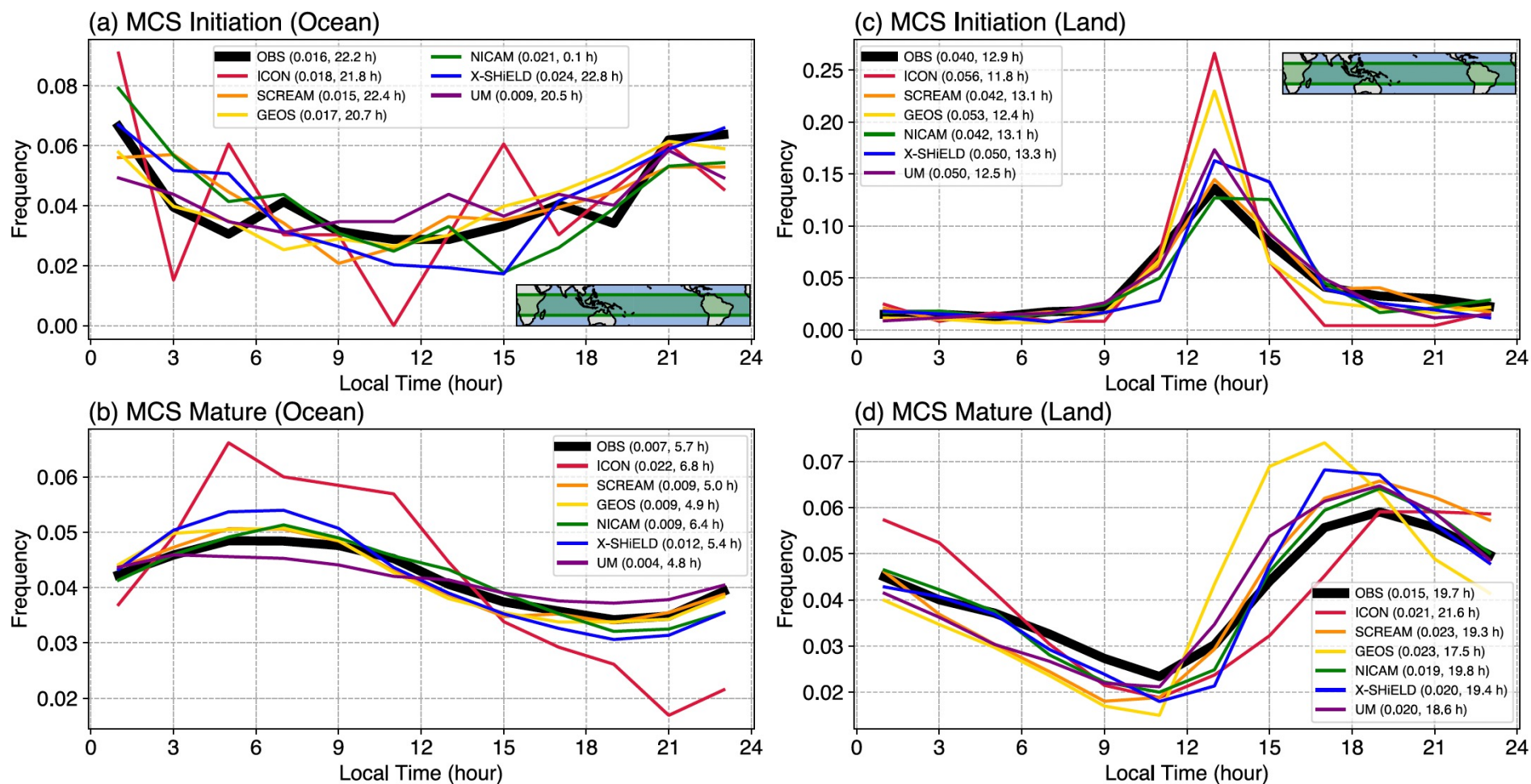


Figure 2. Diurnal cycle of frequencies of tropical MCSs at convection initiation (a),(c) and mature stage (b),(d) over ocean (left column) and land (right column). The amplitude and phase of the diurnal cycles are provided in the legend. Amplitude and phase are calculated using the first harmonic of the Fourier transform applied to the diurnal cycle frequency signal (Wallace, 1975). Area of the tropics included in the analysis is shown as the green box in the inset (20°S – 10°N). An MCS with more than 80% of average PF area fraction over land (ocean) during the first 3 hr of MCS convection initiation is considered a land (ocean) MCS. MCS tracks that start as a split are excluded in this analysis.

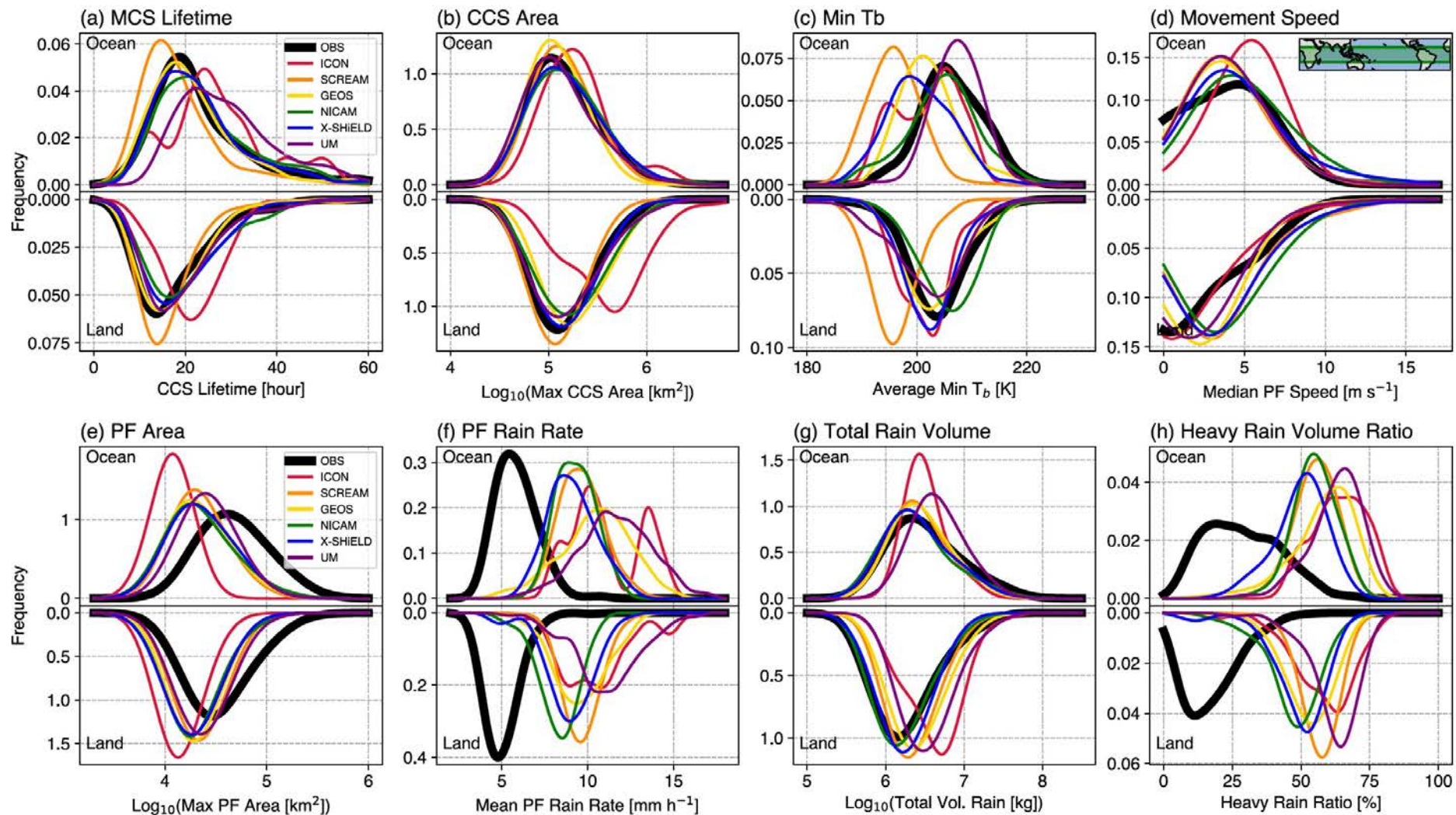
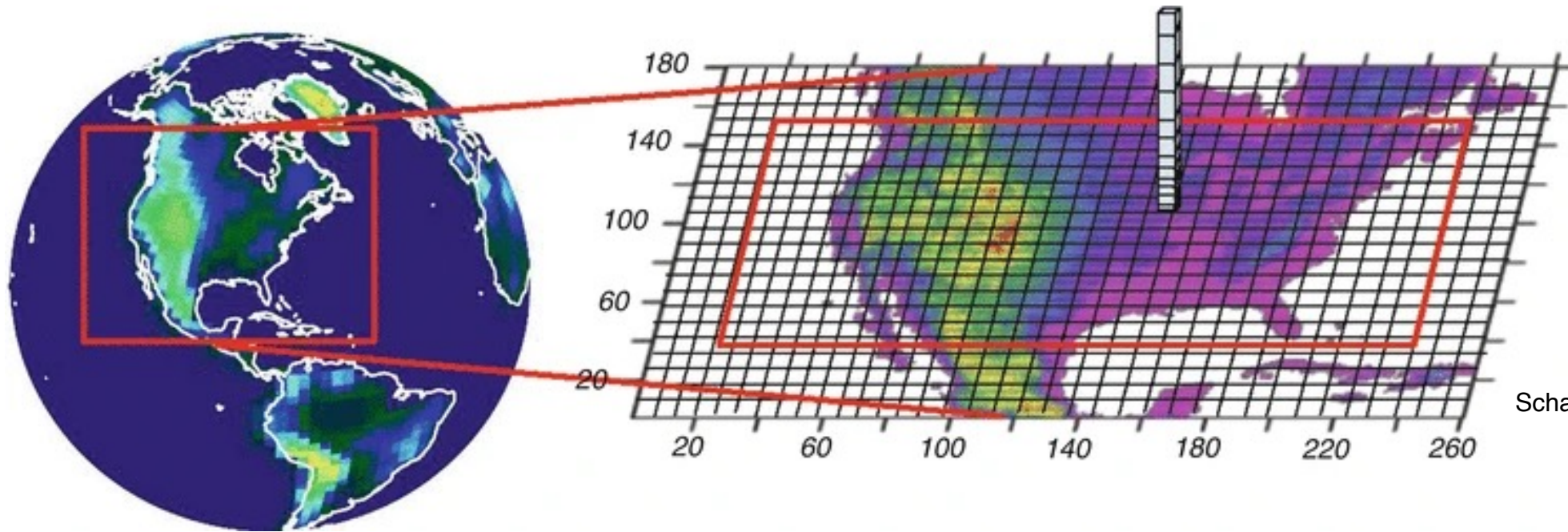


Figure 3. Kernel density estimation of tropical (20°S – 10°N) MCS characteristics from observations (thick black line) and simulations (color lines) over ocean (top half in each panel) and over land (bottom half in each panel). (a) MCS lifetime (defined by CCS), (b) maximum CCS area, (c) lifetime-average minimum T_b , (d) median PF movement speed, (e) maximum PF area, (f) mean PF rain rate, (g) lifetime-total rain volume, and (h) heavy rain (rain rate $>10 \text{ mm hr}^{-1}$) volume ratio (heavy rain volume/total rain volume). All parameters are calculated over the lifetime and within the CCS mask of each MCS.

Pseudo-global warming (PGW) approach



Schar et al. (1996); Sato et al. (2007) ...

change signal for the RCP8.5 scenario. As described in Liu et al. (2016), the WRF input for the PGW simulation is as follows:

$$\text{WRF}_{\text{INPUT}} = \text{ERA} - \text{Interim} + \Delta\text{CMIP5}_{\text{RCP8.5}} \quad (1)$$

where $\Delta\text{CMIP5}_{\text{RCP8.5}}$ is the 95-year CMIP5 multi-model ensemble-mean monthly change under the RCP8.5 scenario:

$$\Delta\text{CMIP5}_{\text{RCP8.5}} = \text{CMIP5}_{2071-2100} - \text{CMIP5}_{1976-2005} \quad (2)$$

The perturbed fields that were used to generate the WRF input for the PGW simulation include horizontal wind, geopotential, temperature, specific humidity, sea surface temperature, soil temperature, sea level pressure, and sea ice. Across the CONUS domain, temperature changes in

未来MCS的变化：10 August 2020 Midwest Derecho

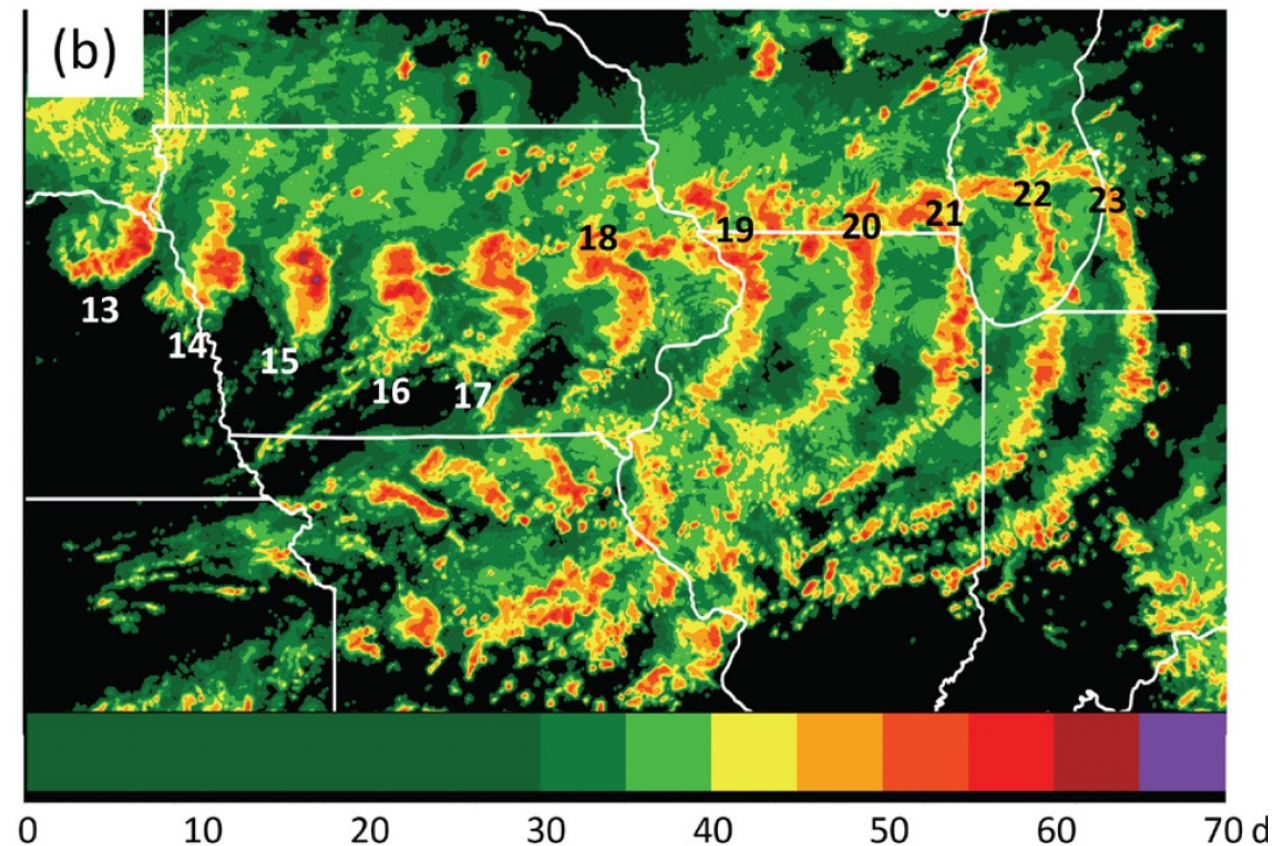
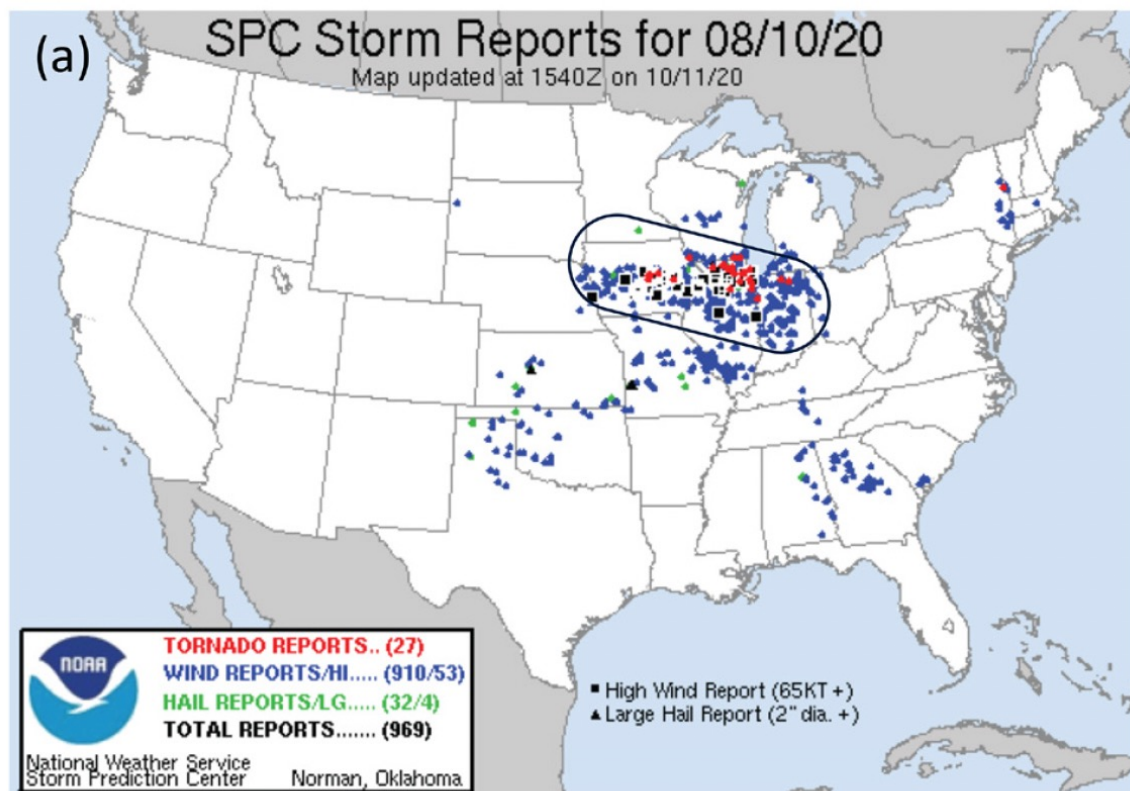


Fig. 1. (a) Hazardous weather reports from the derecho-producing MCS (approximately within black oval) on 10 Aug 2020; reports from other storms that occurred afterward in Missouri area also shown. Blue triangles denote wind reports greater than 50 kt or wind damage; black squares denote significant severe wind reports (>65 kt). (b) Hourly composite radar reflectivity montage of the 10 Aug 2020 derecho-producing MCS from 1300 to 2300 UTC; data from GridRad version 4.2 hourly archive DOI: [10.5065/Y463-4B15](https://doi.org/10.5065/Y463-4B15).

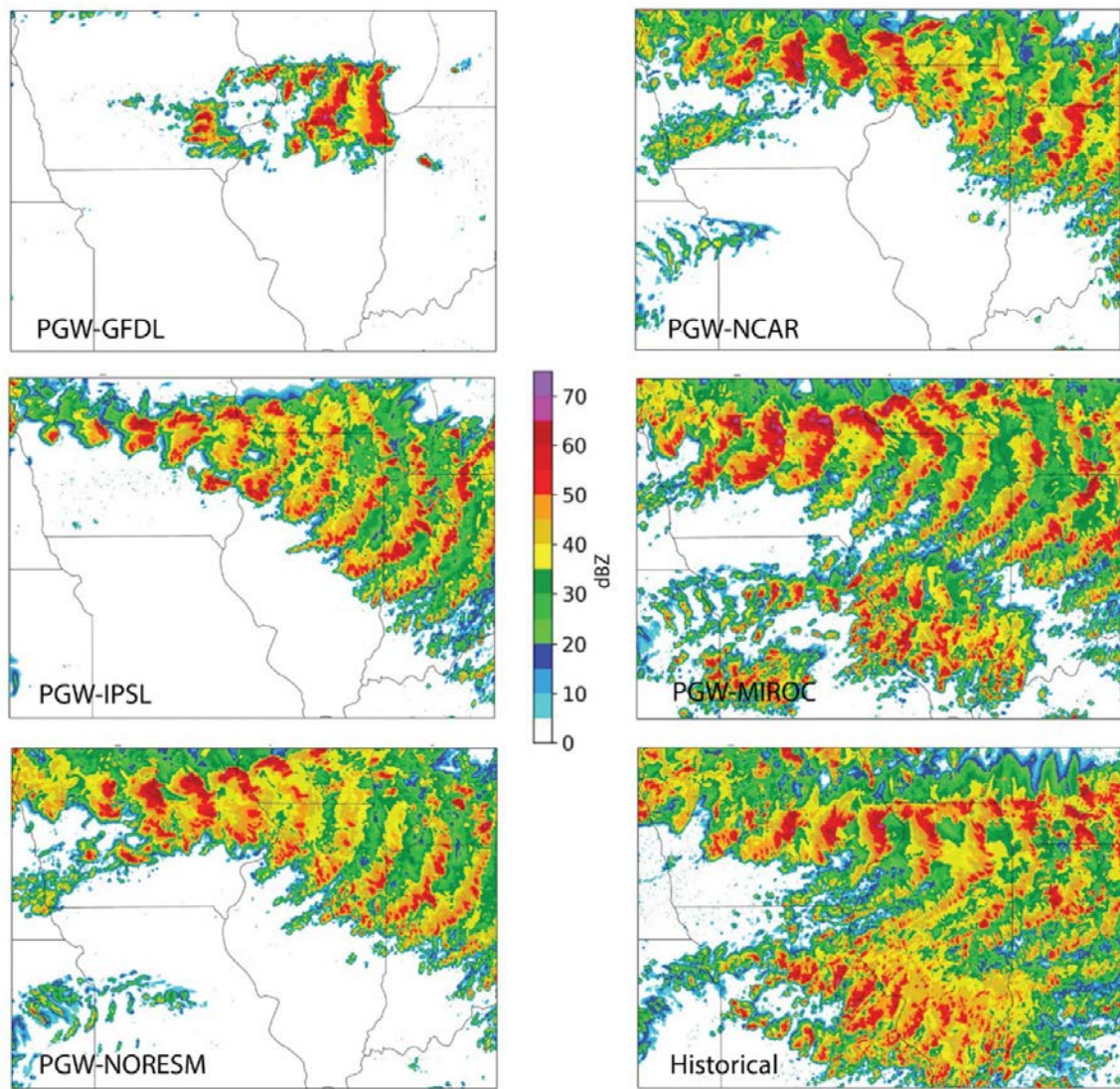


Fig. 8. Hourly simulated column-maximum reflectivity over the nested domain for (bottom right) the historical simulation and all PGW simulations as labeled for the duration of the simulations.

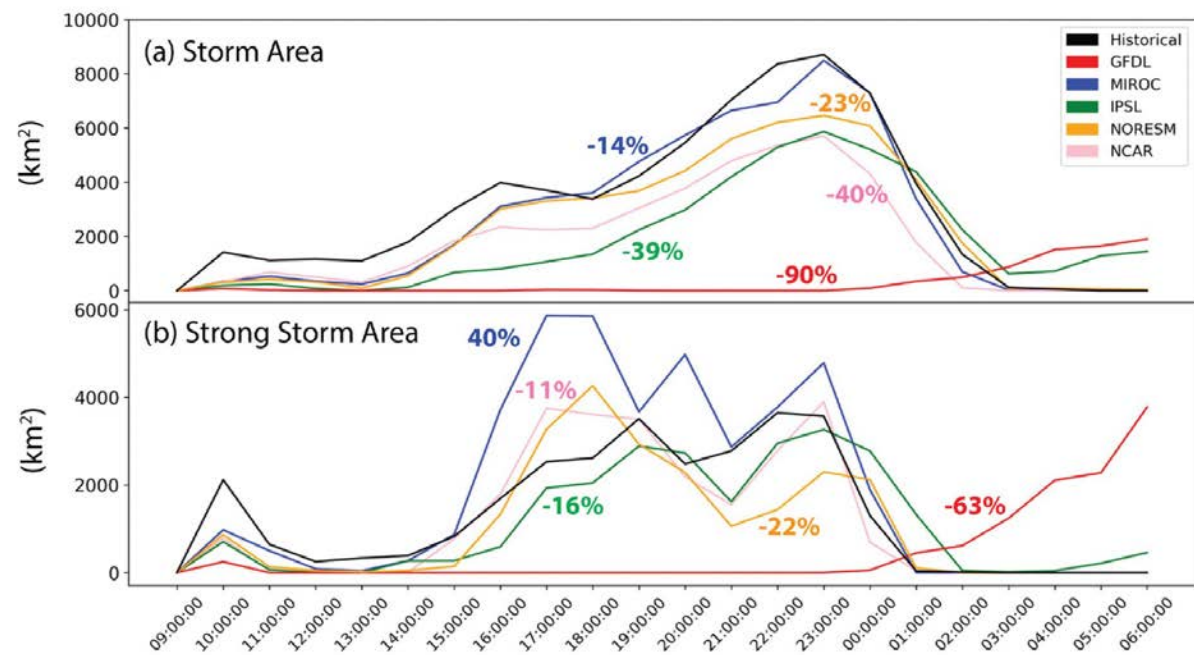


Fig. 9. Time series of hourly (a) simulated total storm area (area over which column-maximum reflectivity exceeded 20 dBZ), and (b) intense storm area (area over which column-maximum reflectivity exceeded 50 dBZ), north of 40°N. HIST simulation shown as black line; PGW simulations shown in other colors. Percentages are time averages relative to HIST, color-coded according to the PGW simulation. All times are in UTC.

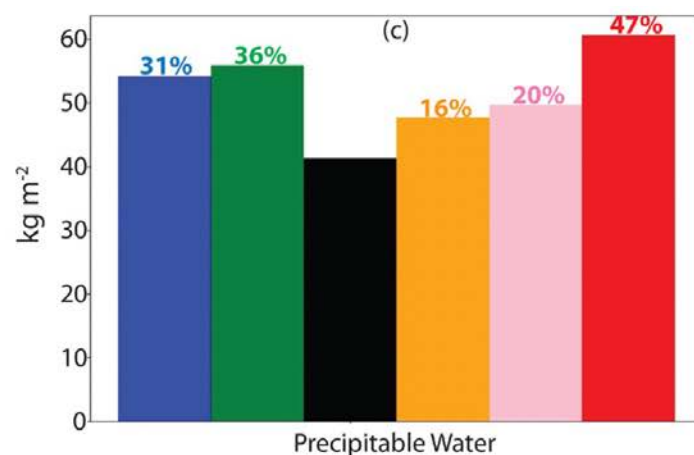
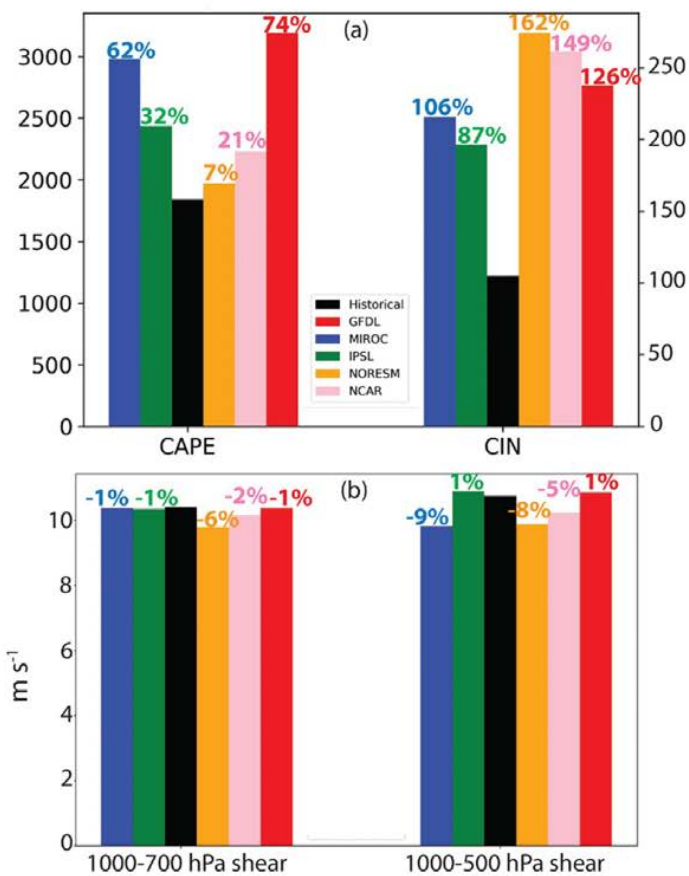


Fig. 6. Meteorological parameters characterizing the changes in potential convective environments averaged over the nested domain of the simulations, evaluated at 1200 UTC over any column having less than a simulated 20 dBZ echo: (a) most unstable CAPE and CIN; (b) lower-tropospheric and low-to-midtropospheric vertical wind shear; (c) precipitable water. Percentages represent changes in PGW relative to HIST.

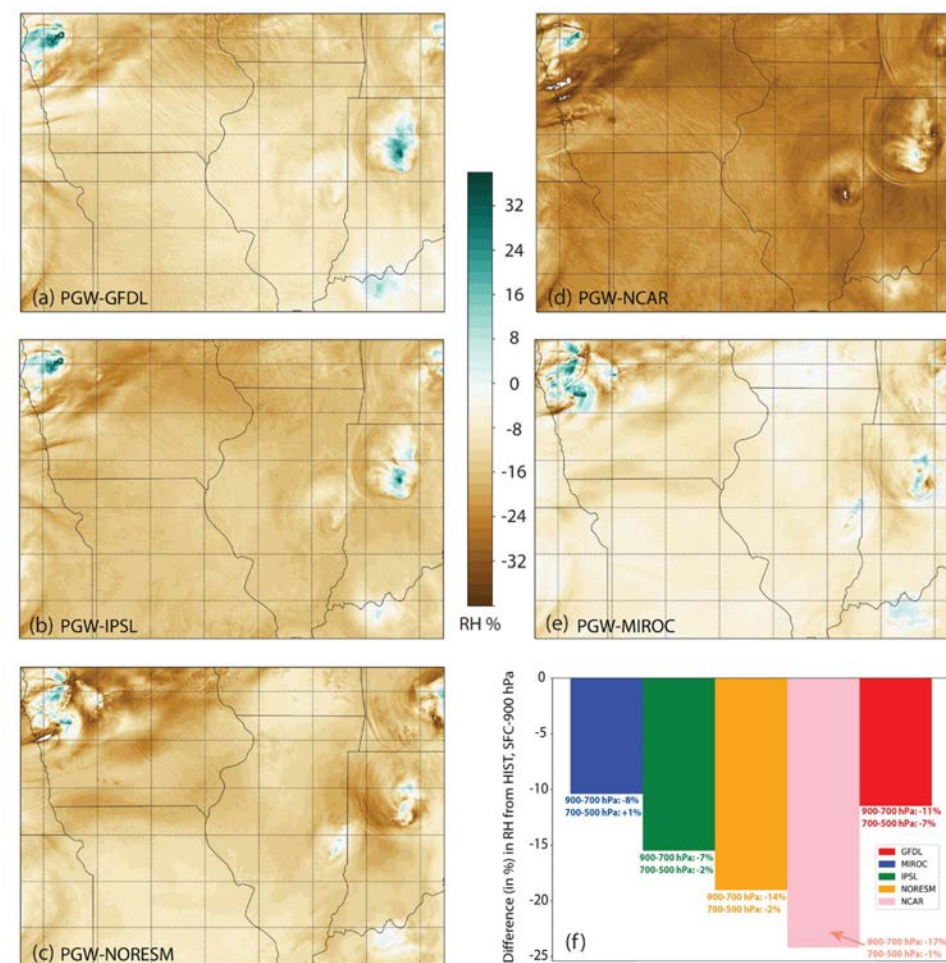


Fig. 7. (a)–(e) Maps of differences in percent of the average surface-to-900-hPa relative humidity in the PGW environments relative to HIST, at 1200 UTC. White/green areas in the plots, including in northwestern Iowa and several areas in the eastern third of the domain, are not valid due to convection being present at those locations at 1200 UTC. (f) Average difference in percent of the surface-to-900-hPa relative humidity from the HIST environment, over the inner domain at 1200 UTC. Labels correspond to same quantities but evaluated over the 900–700 hPa layer or 700–500 hPa layer.

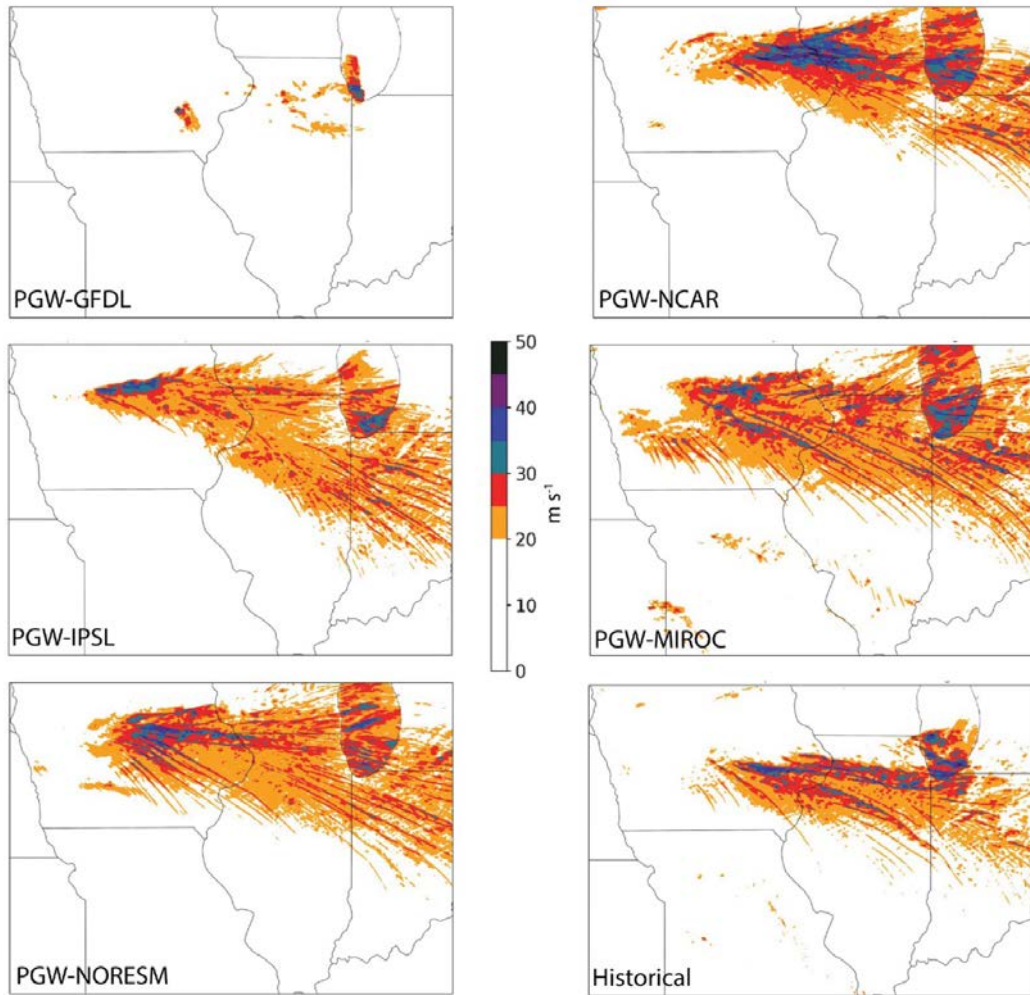


Fig. 10. As in Fig. 8, but for corresponding wind swaths of maximum winds 10m above the ground and 20 m s^{-1} and greater, output by the model at 15-min intervals over the duration of the simulations.

Lasher-Trapp et al. (2023)

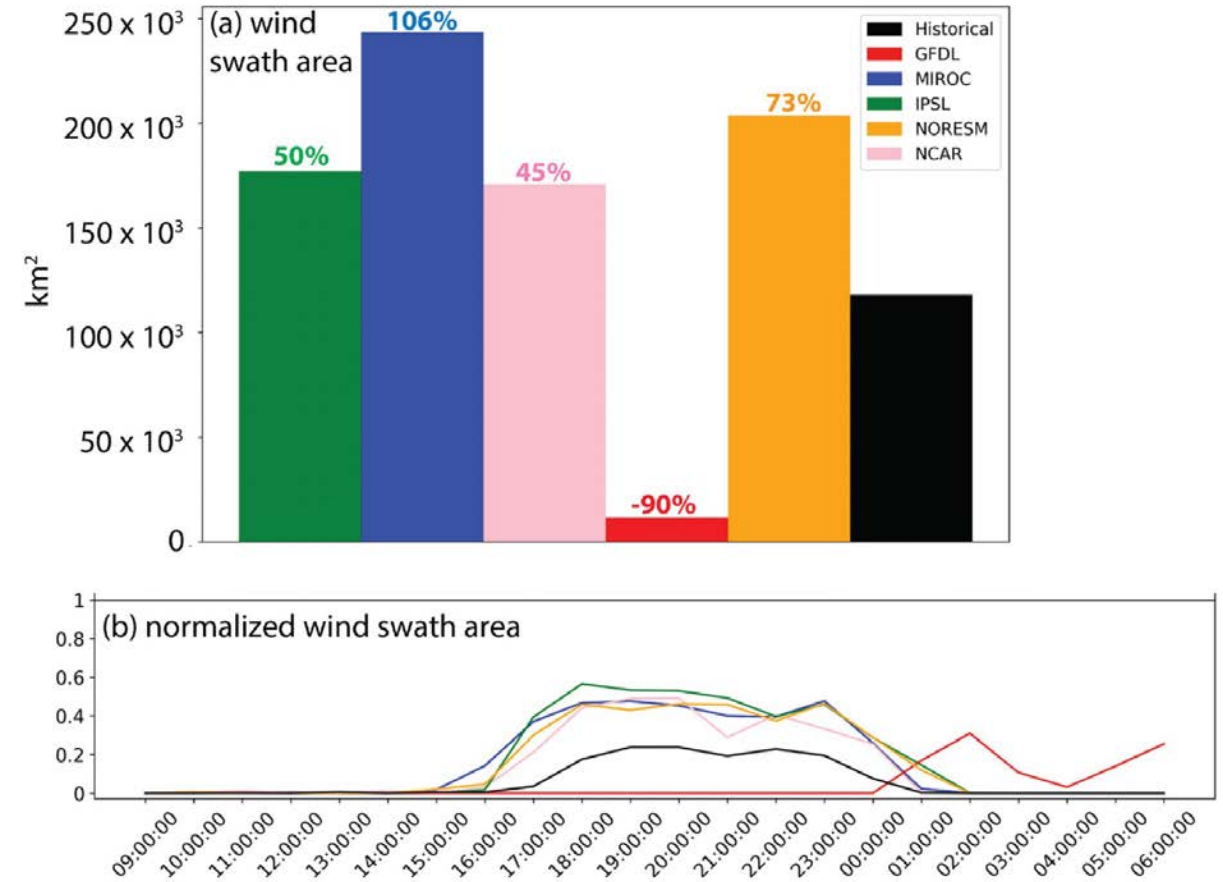


Fig. 11. (a) Total wind swath area, with percentage change relative to HIST simulation shown by the corresponding colors; (b) hourly time series (UTC) of ratio of total area of maximum near-surface wind speeds exceeding 20 m s^{-1} to the total storm area from Fig. 9a, with line colors corresponding to legend in (a). All quantities calculated north of 40°N .

Contradicted results from the other study

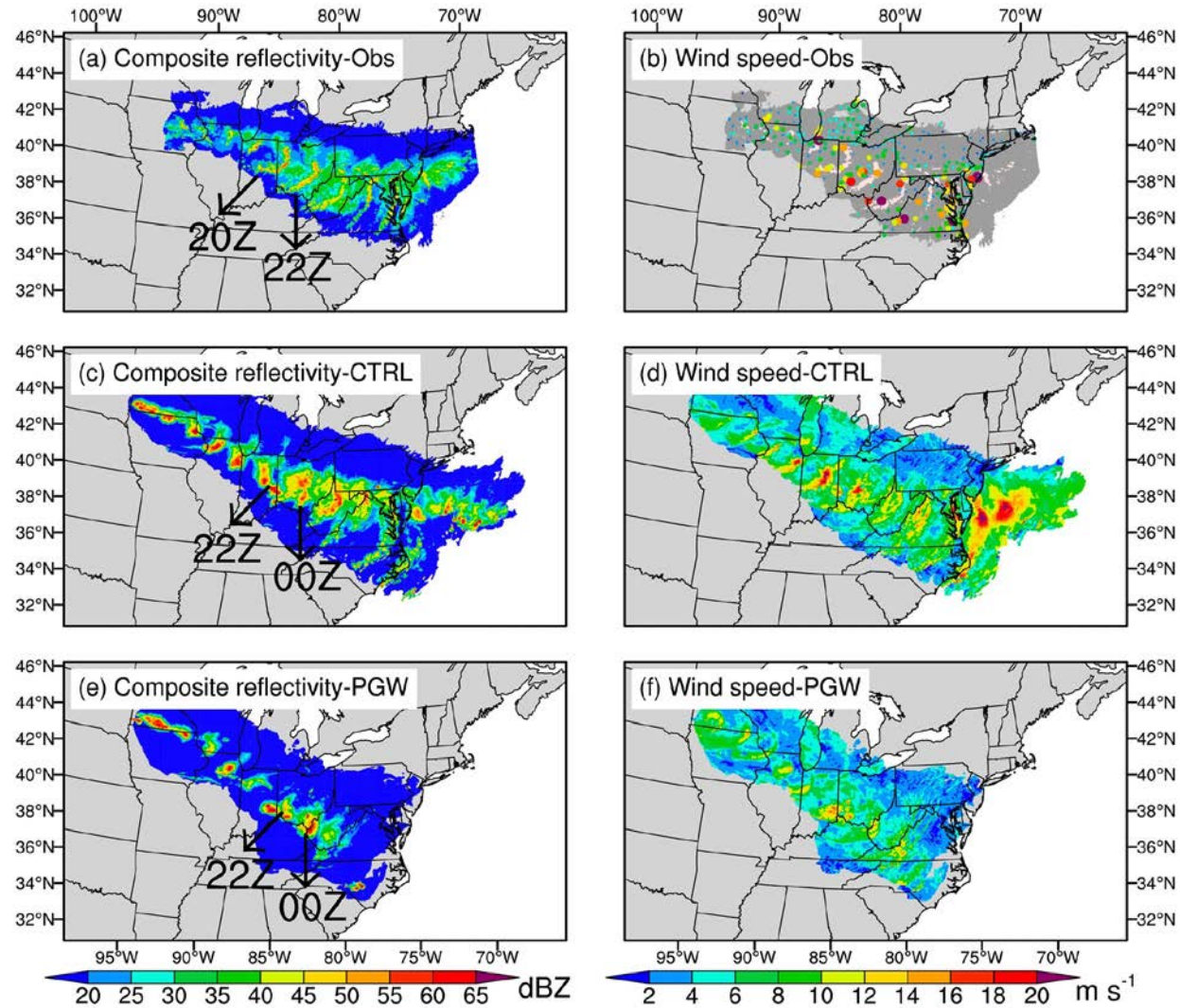



Figure 5. Spatial evolutions of the derecho (a, c, e) radar signatures and (b, d, f) surface wind speeds every other hour for (a, b) observations, (c, d) the CTRL simulations (ensemble mean), and (e, f) the PGW simulations (ensemble mean). We use composite reflectivities to represent radar signatures, some of which are labeled with the corresponding timing of occurrence in (a), (c), and (e). 20Z and 22Z refer to 20:00 and 22:00 on June 29, while 00Z indicates 0:00 on June 30. The dark gray shading in (b) denotes the observed derecho CCS coverage during the selected hours, the same as the blue shading in (a), similar to (c)–(f). The misty rose shading in (b) corresponds to composite reflectivities ≥ 40 dBZ. The point sizes in (b) are proportional to the wind speed magnitudes. Instantaneous winds are plotted in (d) and (f), but (b) displays $wind_{hourly_max}$. This figure does not show all details of the radar signatures and wind features due to the data selection every other hour and potential data overlapping.

Increased rainfall volume from future convective storms in the US

Andreas F. Prein *, Changhai Liu, Kyoko Ikeda, Stanley B. Trier, Roy M. Rasmussen, Greg J. Holland and Martyn P. Clark

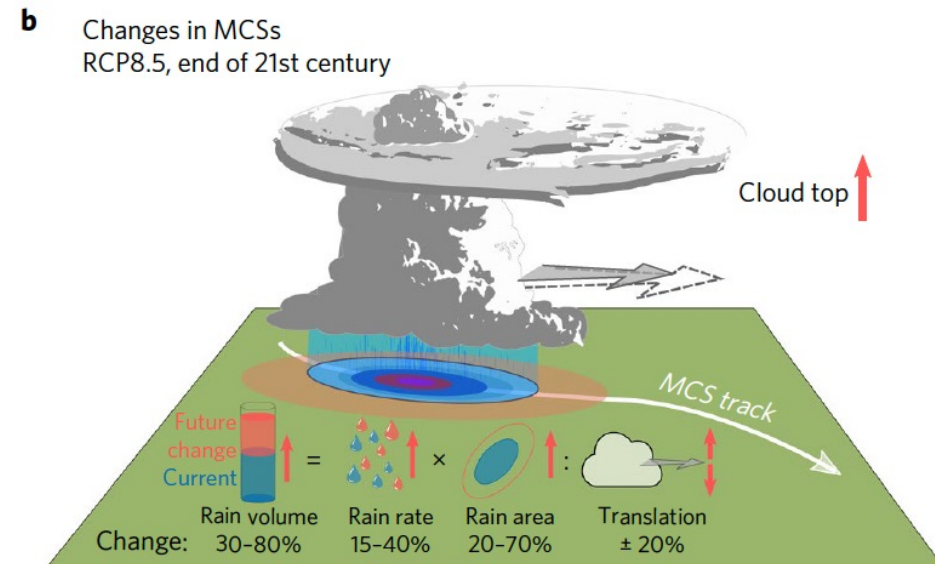
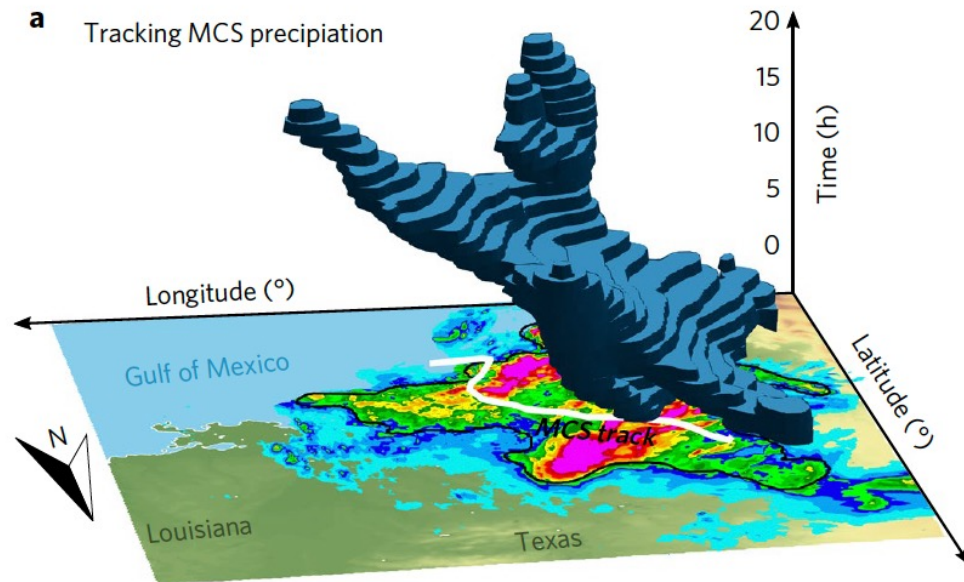


Fig. 1 | Schematic of Lagrangian tracking of MCS precipitation and future changes in MCSs. a, MCS hourly precipitation accumulations above 5 mm h^{-1} are identified and tracked over space and time (time corresponds to the vertical axis). **b**, Characteristics such as storm motion, rain rates or cloud top heights are identified for MCSs in the current and future climate. Highest increases are found for MCS precipitation volumes, which is positively related to increasing rain rates and rain areas and negatively to changes in storm motion (**b**).

Table 1 | **Summary of changes in MCS properties with warming**

Variable	Sign of change	Confidence ^a	Refs
<i>MCS characteristics and hazards</i>			
Rainfall (rate and volume)	Increase	High	16–18,119,165, 171,172,185
Severe winds	Uncertain ^b	–	177
Speed of motion	Increase	Low	16
Organization	Uncertain ^b	–	16,17,119,173
Size	Increase	Medium	16,17,119,185
Frequency	Increase	Low	16,165,173
<i>MCS environments</i>			
Atmospheric moisture	Increase	High	14,15,177–181
Atmospheric instability	Increase	High	14,15,177–181
Convective inhibition	Increase	Medium	14,181
Vertical wind shear	Uncertain ^b	–	15,176,178
Frequency of environments supportive of MCSs	Increase	Low	15,17,165, 178,181

MCS, mesoscale convective system. ^aConfidence refers to the convergence of evidence based on different data sources and lines of inquiry. Confidence is rated as high for results that have been consistently found across numerous studies with both theoretical and modelling support.

^bUncertainty arises owing to inadequate investigation and, as such, there is no estimate of confidence. For MCS organization, there is confidence that changes will occur, but there is uncertainty in what those changes will be, including the sign.